INTERNATIONAL JOURNAL FOR NUMERICAL METHODS IN FLUIDS
Int. J. Numer. Meth. Fluids 2008; **57**:355–387
Published online 25 October 2007 in Wiley InterScience (www.interscience.wiley.com). DOI: 10.1002/fld.1586

Positive-definite q-families of continuous subcell Darcy-flux CVD(MPFA) finite-volume schemes and the mixed finite element method

Michael G. Edwards*, † and Mayur Pal

Civil and Computational Engineering Centre, University of Wales, Swansea SA2 8PP, U.K.

SUMMARY

A new family of locally conservative cell-centred flux-continuous schemes is presented for solving the porous media general-tensor pressure equation. A general geometry-permeability tensor approximation is introduced that is piecewise constant over the subcells of the control volumes and ensures that the local discrete general tensor is elliptic. A family of control-volume distributed subcell flux-continuous schemes are defined in terms of the quadrature parametrization q (*Multigrid Methods*. Birkhauser: Basel, 1993; *Proceedings of the 4th European Conference on the Mathematics of Oil Recovery*, Norway, June 1994; *Comput. Geosci.* 1998; **2**:259–290), where the local position of flux continuity defines the quadrature point and each particular scheme. The subcell tensor approximation ensures that a symmetric positive-definite (SPD) discretization matrix is obtained for the base member ($q=1$) of the formulation. The physical-space schemes are shown to be non-symmetric for general quadrilateral cells. Conditions for discrete ellipticity of the non-symmetric schemes are derived with respect to the local symmetric part of the tensor. The relationship with the mixed finite element method is given for both the physical-space and subcell-space q-families of schemes. M-matrix monotonicity conditions for these schemes are summarized. A numerical convergence study of the schemes shows that while the physical-space schemes are the most accurate, the subcell tensor approximation reduces solution errors when compared with earlier cell-wise constant tensor schemes and that subcell tensor approximation using the control-volume face geometry yields the best SPD scheme results. A particular quadrature point is found to improve numerical convergence of the subcell schemes for the cases tested. Copyright © 2007 John Wiley & Sons, Ltd.

Received 31 December 2005; Revised 27 June 2007; Accepted 2 July 2007

KEY WORDS: convergence; subcell; family of flux-continuous finite-volume schemes; permeability tensor; quadrature parametrization and pressure equation; CVD; MPFA; mixed finite element methods

*Correspondence to: Michael G. Edwards, Civil and Computational Engineering Centre, School of Engineering, University of Wales Swansea, Singleton Park Swansea, SA2 8PP Wales, U.K.
†E-mail: m.g.edwards@swansea.ac.uk

Contract/grant sponsor: EPSRC; contract/grant number: GR/S70968/01
Contract/grant sponsor: ExxonMobil Upstream Research Company

1. INTRODUCTION

Continuous flux and pressure discretization of the reservoir simulation pressure equation are required in order to honour correct local physical interface conditions between grid blocks with strong discontinuities in permeability. Rapid variation in permeability is common in subsurface reservoirs.

The derivation of local algebraic flux continuity conditions for full tensor discretization operators has lead to efficient and robust locally conservative q-families of flux-continuous finite-volume schemes for determining the discrete pressure and velocity fields in subsurface reservoirs [1–9], where they are called flux-continuous control-volume distributed (CVD) schemes. Closely related work that has focused on a single member of the q-family (given by $q=1$) is presented in [10–12], where they are called multi-point flux approximation (MPFA) methods, schemes of this type are also presented in [13–15]. All of the above CVD(MPFA) schemes are applicable to the diagonal and full tensor pressure equation with generally discontinuous coefficients and remove the $O(1)$ error introduced by standard reservoir simulation schemes when applied to full tensor flow approximation while maintaining a single degree of freedom per control volume. Coupling of the flux-continuous schemes with higher order convective flux approximations applied to multi-phase flow on structured and unstructured grids in two and three dimensions is presented in [16, 17], respectively.

Other schemes that preserve flux continuity have been developed from variational frameworks, using the mixed finite element (MFE) method, e.g. [18–23] and related work [24]. More recently discontinuous Galerkin (DG) formulations have been presented, e.g. [25–27] which apply to non-matching grids and permit an increase in order of accuracy. However, the MFE and DG methods introduce further degrees of freedom which increase the size of the global system matrix when compared with the methods presented here.

Here, we begin with the family of flux-continuous, locally conservative, CVD(MPFA) finite-volume schemes presented in [3, 5, 8]. These schemes have been developed for solving the general geometry-permeability tensor pressure equation on structured and unstructured cell-centred and cell vertex grids and are CVD. The family of locally conservative flux-continuous schemes is built on the underlying principles of continuity in normal flux and pressure.

The first numerical convergence study of the family of flux-continuous schemes in *physical* space, with emphasis on variable quadrature point (defining the position of continuity) is presented in [8]. A range of quadrature points is tested and the benefit of using a specific *quadrature point* is identified, with good convergence results for some challenging cases. However, the formulation of the family of flux-continuous finite-volume schemes in *physical* space leads to discretization matrices that are not necessarily symmetric in the general case for both quadrilateral and triangular grids [6, 7], though it is shown here that the *physical*-space flux-continuous schemes can still be positive definite subject to ellipticity of the symmetric part of the physical-space tensor.

Alternative formulations that yield symmetric positive-definite (SPD) discretization matrices have been derived in transform space. The first schemes were cell centred and introduced local piecewise constant general-tensor T approximations over the cell or control volume [3, 12] for structured grids. The second set of schemes are vertex based and introduce piecewise constant general-tensor approximations over the *subcells* of each control volume [5–7], where the schemes are developed for structured and unstructured grids and are shown to be SPD for any grid (for base quadrature $q=1$). These formulations achieve SPD discretization by introduction of an additional local approximation in geometry. The relationship between the CVD(MPFA) schemes and the

DOI: 10.1002/fld

mixed finite element method was first presented in [5] for $q=1$ and is used in [28] in a convergence proof of MPFA, also discussed in [29].

This paper continues with the developments presented in [6, 7, 30] applied in a cell-centred framework. A comparison of convergence rates is presented for *physical* space *versus* cellwise transform-space and subcell transform-space flux-continuous formulations with focus on both the effect of the local subcell tensor approximation and the effect of different quadrature rules [8]. In this study, the subcell schemes are formulated with respect to cell-centred flow and rock variables where control volumes are the primal quadrilateral grid cells. The base ($q=1$) subcell CVD(MPFA) scheme is shown to yield a discretization matrix which is SPD. The relationship between the new formulations, the earlier physical-space flux-continuous schemes and the MFE method is also established here for the q-families of schemes.

This paper is organized as follows: Section 2 describes the single-phase flow problem encountered in reservoir simulation with respect to the general-tensor pressure equation. An overview of the family of physical-space flux-continuous finite-volume schemes for 2D quadrilateral grids is given in Section 3. The quadrature parametrization which defines the family of flux-continuous schemes is also given. General positive-definite conditions are derived in Section 4. Subcell tensor approximations are presented in Section 5. The subcell family of flux-continuous schemes are defined in Section 6. The relationships between the physical-space schemes, subcell space schemes and the MFE method are presented in Section 7. A summary of monotonicity conditions is given in Section 8. Numerical convergence results for the physical space, cellwise transform-space and subcell transform-space schemes are presented for a range of quadrature points in Section 9. Conclusions are given in Section 10.

2. FLOW EQUATIONS

While the methods presented are for both single-phase and multi-phase flow problems, the focus here is on robust finite-volume approximation of the pressure equation on general quadrilateral grids. The pressure equation is defined in terms of a general curvilinear coordinate system parametrized with respect to a uniform dimensionless transform space with an (ξ,η) coordinate system. Choosing Ω to represent an arbitrary control volume composed of surfaces that are tangential to constant (ξ,η), respectively, the integral form of the pressure equation is written as

$$\int_{\Omega} \nabla\cdot\mathbf{V}\,\mathrm{d}\tau = -\oint_{\partial_\Omega} \mathbf{K}\nabla\phi\cdot\hat{\mathbf{n}}\,\mathrm{d}s = M \tag{1}$$

where $\mathbf{V}=-\mathbf{K}\nabla\phi$ is the Darcy velocity, $\mathbf{K}$ is the elliptic permeability tensor, $\partial\Omega$ is the boundary of Ω, $\hat{n}$ is the unit outward normal and ϕ is the pressure, and M is a source term (or flow rate) which is zero away from well locations. Spatial derivatives are calculated using

$$\phi_x = J(\phi,y)/J(x,y), \quad \phi_y = J(x,\phi)/J(x,y) \tag{2}$$

where $J(x,y)=x_\xi y_\eta - x_\eta y_\xi$ is the Jacobian. The flux in Equation (1) is now resolved along the outward normals to constants ξ and η respectively, where normal increments are

$$\mathbf{n1}=\hat{\mathbf{n1}}\,\mathrm{d}s_1=(y_\eta,-x_\eta)\,\mathrm{d}\eta, \quad \mathbf{n2}=\hat{\mathbf{n2}}\,\mathrm{d}s_2=(-y_\xi,x_\xi)\,\mathrm{d}\xi \tag{3}$$

DOI: 10.1002/fld

This gives rise to the general-tensor form of the pressure equation

$$\oint_{\partial\Omega_p} \mathbf{V}\cdot\hat{\mathbf{n}}\,\mathrm{d}s = \oint_{\partial\Omega_p} (u\,\mathrm{d}y - v\,\mathrm{d}x) = \sum_{i=1}^{2} \Delta_i F_i = M \tag{4}$$

with $\mathbf{V}=(u,v)$, the outward normal flux is given by

$$F_i = -\int \sum_{j=1}^{2} \mathbf{T}_{i,j}\phi_{\xi_j}\,\mathrm{d}\Gamma_i \tag{5}$$

where $\mathrm{d}\Gamma_i$ is the ith parametric coordinate surface increment and ϕ_{ξ_j} is the derivative of ϕ with respect to ξ_j. The $T_{i,j}$ are components of the resulting general elliptic tensor

$$\mathbf{T} = J\mathbf{J}^{-1}\mathbf{K}\mathbf{J}^{-\mathrm{T}} \tag{6}$$

(also known as the Piola transform) which is in turn a function of the Cartesian permeability tensor $\mathbf{K}$ and geometry *via* $\mathbf{J}$, where $\mathbf{J}=\partial\mathbf{x}/\partial\boldsymbol{\xi}$ is the Jacobian of the coordinate transformation. Full tensors can arise from local orientation and distortion of the grid, when using unstructured grids, upscaling and local orientation of the permeability field. The boundary conditions used are either Dirichlet (specifying pressure, which is always applied for at least one point in or on the boundary of Ω), and/or Neumann (specifying flux).

3. FAMILY OF FLUX-CONTINUOUS FINITE-VOLUME SCHEMES (PHYSICAL SPACE)

Local conservation, flux and pressure continuity are key physical properties satisfied by the exact solution of Equation (1). Local conservation is the basis upon which every finite-volume scheme is built and relies on a flux balance, where relative to a given control-volume face, flux is subtracted from the left volume and the same flux is added to the right volume. We note that while flux continuity ensures local conservation, the converse is not necessarily true and CVFE is a case in point. Consequently, we must therefore build flux continuity into the approximation of Equation (1). Families of *physical* space and transform-space flux-continuous CVD(MPFA) finite-volume schemes are presented in [1–8] for different grid types. Numerical convergence rates of the families of schemes on structured and unstructured grids using a range of quadrature rules are presented in [8].

In this section, we present the framework for the physical-space formulation specialized to cell-centred quadrilateral grids. The subcell space formulation is then described within the same framework in the following section so that the distinctions between methods are made clear.

The nine-node support of the scheme is indicated in Figure 1(a). The scheme has cell-centred flow and rock variables, so that the approximation points (or nodes) are shared by both variables and are at the centres of the primal grid cells. Thus, in this case the primal grid cells are the control volumes and the schemes are CVD with respect to the primal grid cells as shown in Figure 1(c), where the central control volume is the cell with vertex (corner) position vectors $\mathbf{r}_{V_1}, \mathbf{r}_{V_2}, \mathbf{r}_{V_3}, \mathbf{r}_{V_4}$, and the scheme is centred on node 1.

Dual cell: Each group of four cell-centred nodes surrounding a primal grid vertex defines the fundamental corners of a *dual cell*, as indicated by the dashed line in Figure 1(b). The perimeter of each dual cell is defined by joining cell centres to cell edge mid-points as in Figure 1(b).

DOI: 10.1002/fld

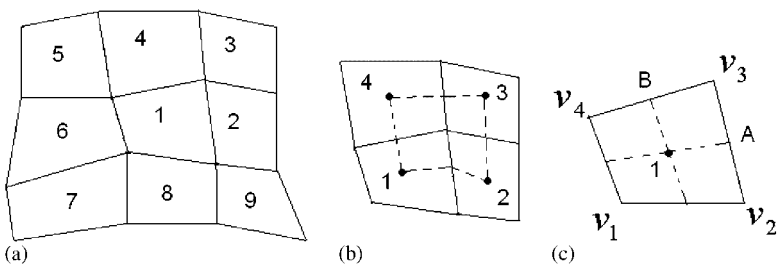

Figure 1. (a) Nine-point scheme support; (b) dual-cell (dashed line); and (c) four subcells of cell 1, vertices V_i, $i=1,\ldots,4$.

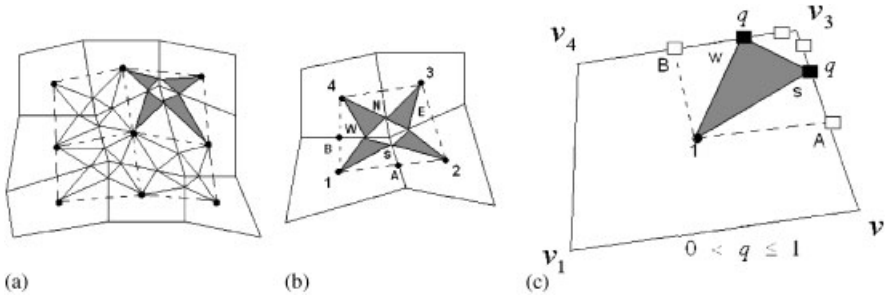

Figure 2. (a) Nine-point continuous pressure support, highlighted *dual-cell* dashed line; (b) points of flux-continuity (N, S, E, W) on subcell faces in the *dual cell*; and (c) cell 1 and example quadrature points $q=0.1$, $q=1$ hollow squares (on subcell faces): general q bold squares.

Subcells: The dual cells partition the primal quadrilateral grid cells (or control volumes) into sub-quadrilateral cells, which are called subcells [5]. Each control volume and each dual cell (Figure 1(b)) comprised four subcells. Each subcell has one corner attached to a cell centre node and the opposite corner attached to a control-volume corner (a primal grid vertex). A subcell is illustrated in Figure 1(c) with corner position vectors $\mathbf{r}_1, \mathbf{r}_A, \mathbf{r}_{V_3}, \mathbf{r}_B$. The two faces of a subcell attached to the primal grid vertex define two *sub-faces* of a parent control volume, refer to the top right corner of the cell in Figure 1(c), with sub-faces (A, V_3) and (V_3, B) over which $(0<q\leqslant 1]$; see q-family below.

Pressure sub-triangles: Pressure sub-triangles are defined within subcells as follows: interface pressures $\phi_N, \phi_S, \phi_E, \phi_W$ are introduced on the four *sub-faces* inside each dual cell at specified positions (N, S, E, W), as defined in Figure 2(b). Sub-triangles are then formed by connecting cell centres to the interface pressure positions and the sub-triangles indicate local piecewise linear support of pressure. For example, Figure 2(c) shows cell 1 (the central pressure node) and a subcell with sub-triangle $(1, S, W)$ inside the subcell, continuity points (S, W) are indicated by solid squares. Introduction of interface pressures $\phi_N, \phi_S, \phi_E, \phi_W$ (Figure 2(b)) automatically ensures point-wise pressure continuity across control-volume interfaces in a locally coupled system. Pressure gradients are, therefore, piecewise constant over the sub-triangles and are linear functions of discrete cell-centre and cell interface pressures.

DOI: 10.1002/fld

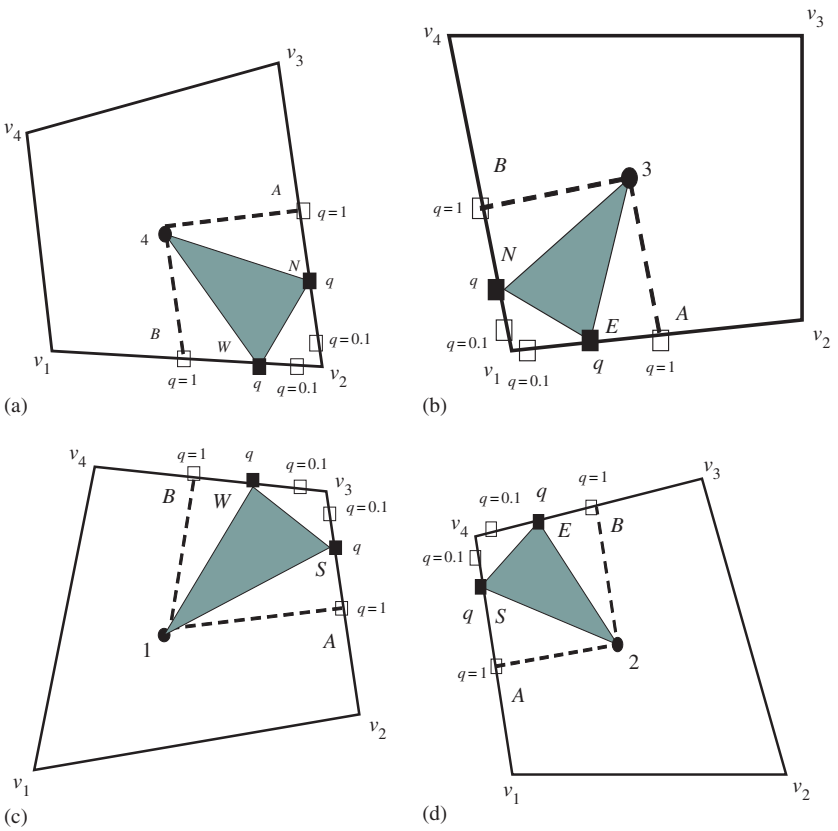

Figure 3. Quadrature parametrization on the subcell faces—exploded view of Figure 2(b): example of quadrature points $q=0.1, 1$ hollow squares: general q solid squares.

q-Family of schemes—quadrature parametrization: The family of schemes is formed when imposing normal flux and pressure continuity conditions at the four positions (N, S, E, W), (Figure 2(b)) on the *sub-faces*, where the four shaded triangles meet in a dual cell. On each *sub-face*, the point of continuity is parametrized with respect to the subcell by the variable q, where $(0<q\leqslant 1]$. Families of flux-continuous schemes were first introduced by Edwards and Rogers [1–3]. Here, in addition to establishing conditions for general positive definiteness, we continue to explore the effects of different quadrature values, q, on scheme performance. Specific quadrature points $q=0.1, 1$ are illustrated in Figure 3 (hollow squares) together with the subcell triangle construction for a generic value of q (solid squares). Results from using different quadrature points are compared in the results section. For a given subcell, the points of continuity can lie anywhere in the intervals $(0<q\leqslant 1]$ on the two faces of a subcell inside a dual cell, that coincide with the control-volume *sub-faces*, and the value of q defines the quadrature point and hence the family of flux-continuous finite-volume schemes.

The parametric variation in q is illustrated further using the subcell example of Figure 2(c), with subcell containing sub-triangle $(1, S, W)$. Let $\mathbf{r}_1=(x_1, y_1)$ denote the coordinates of the

DOI: 10.1002/fld

cell centre and $\mathbf{r}_S=(x_S, y_S)$, $\mathbf{r}_W=(x_W, y_W)$ denote the local continuity coordinates. Then it is understood that the continuity position is a function of q with $\mathbf{r}_S(q)$ and $\mathbf{r}_W(q)$. As noted in [2], a different parametric value can also be chosen along each sub-face so that $\mathbf{r}_S(q_1)$ and $\mathbf{r}_W(q_2)$ will be presented in a future report [31].

Piecewise constant Darcy fluxes are now constructed on each of the pressure sub-triangles belonging to the subcells of the *dual cell* as shown in Figure 2(b). The local linear pressure, $\phi=\phi_1+(\phi_S-\phi_1)\xi+(\phi_W-\phi_1)\eta$, is expanded in (ξ, η) sub-triangle basis function coordinates. The Darcy-flux approximation is illustrated for sub-triangle $(1, S, W)$, where

$$\begin{pmatrix}\phi_\xi\\ \phi_\eta\end{pmatrix}=\begin{pmatrix}\phi_S-\phi_1\\ \phi_W-\phi_1\end{pmatrix} \tag{7}$$

and

$$\begin{pmatrix}x_\xi(q)\\ x_\eta(q)\end{pmatrix}=\begin{pmatrix}x_S(q)-x_1\\ x_W(q)-x_1\end{pmatrix},\quad \begin{pmatrix}y_\xi(q)\\ y_\eta(q)\end{pmatrix}=\begin{pmatrix}y_S(q)-y_1\\ y_w(q)-y_1\end{pmatrix} \tag{8}$$

Using Equations (7), (8) the discrete Darcy velocity is defined as

$$v_h=-\mathbf{K}\nabla\phi_h=-\mathbf{K}\mathbf{G}(q)\begin{pmatrix}\phi_\xi\\ \phi_\eta\end{pmatrix} \tag{9}$$

where $\mathbf{K}$ is the local permeability tensor of cell 1 and dependency of $\nabla\phi_h$ on quadrature point arises through

$$\nabla\phi_h=\mathbf{G}(q)\begin{pmatrix}\phi_\xi\\ \phi_\eta\end{pmatrix}=\begin{pmatrix}y_\eta(q) & -y_\xi(q)\\ -x_\eta(q) & x_\xi(q)\end{pmatrix}\frac{1}{J(q)}\begin{pmatrix}\phi_S-\phi_1\\ \phi_W-\phi_1\end{pmatrix} \tag{10}$$

where approximate $\mathbf{r}_\xi(q)$ and $\mathbf{r}_\eta(q)$ are defined by Equation (8). Note that (x_1, y_1) is the position vector of the cell centre of cell 1 in Figure 1, and $\mathbf{r}_{V_3}=(x_{V_3}, y_{V_3})$ is the position vector of the corner vertex V_3 of the cell. The normal physical-space flux at the left-hand side of S (Figure 2(b)), is resolved along the outward normal vector $\mathrm{d}L_S=\frac{1}{2}((y_{V_3}-y_{V_2}), -(x_{V_3}-x_{V_2}))$ and is expressed in terms of the general tensor $T=T(q)$ as

$$F_S^1=v_h\cdot\mathrm{d}L_S=-(T_{11}^1\phi_\xi+T_{12}^1\phi_\eta)|_S^1 \tag{11}$$

where it is understood that the coefficients of $-(\phi_\xi, \phi_\eta)|_S^1$, resulting from velocity resolution on $\mathrm{d}L_S$, denoted by $T_{11}|_S^1$ and $T_{12}|_S^2$, are subcell (physical-space) approximations of the general-tensor components (Equation (6)) at the left-hand face at S and are functions of q. A similar expression for flux is obtained at the right-hand side of S from cell 2 (Figure 2(b)). Similarly, subcell fluxes are resolved on the two sides of the other faces at W, N and E. Flux continuity is then imposed across the four cell interfaces at the four positions N, S, E and W (Figure 2(b)) which are

DOI: 10.1002/fld

specified according to quadrature point q. The local *physical*-space flux continuity conditions are now defined with respect to each dual cell and expressed as

$$\begin{aligned} F_N &= -(T_{11}\phi_\xi + T_{12}\phi_\eta)|_N^3 = -(T_{11}\phi_\xi + T_{12}\phi_\eta)|_N^4 \\ F_S &= -(T_{11}\phi_\xi + T_{12}\phi_\eta)|_S^1 = -(T_{11}\phi_\xi + T_{12}\phi_\eta)|_S^2 \\ F_E &= -(T_{12}\phi_\xi + T_{22}\phi_\eta)|_E^2 = -(T_{12}\phi_\xi + T_{22}\phi_\eta)|_E^3 \\ F_W &= -(T_{12}\phi_\xi + T_{22}\phi_\eta)|_W^1 = -(T_{12}\phi_\xi + T_{22}\phi_\eta)|_W^4 \end{aligned} \tag{12}$$

where, for example,

$$-(T_{11}\phi_\xi + T_{12}\phi_\eta)|_S^1 = -(T_{11}|_S^1\phi_\xi|^1 + T_{12}|_S^1\phi_\eta|^1) \tag{13}$$

and $T|_\sigma^i$ denotes the *physical*-space tensor approximation as a function of quadrature point q for subcell i and interface point $\sigma = \sigma(q)$, resulting from normal Darcy velocity resolution on the control-volume faces.

Using Equations (7)–(10) together with the corresponding expansions for the other gradients over each sub-triangle in the dual cell, Equation (12) that holds for any q can be expressed explicitly with respect to potential differences as

$$\begin{aligned} F_N &= -(T_{11}|_N^4(\phi_N - \phi_4) + T_{12}|_N^4(\phi_4 - \phi_W)) = -(T_{11}|_N^3(\phi_3 - \phi_N) + T_{12}|_N^3(\phi_3 - \phi_E)) \\ F_S &= -(T_{11}|_S^1(\phi_S - \phi_1) + T_{12}|_S^1(\phi_W - \phi_1)) = -(T_{11}|_S^2(\phi_2 - \phi_S) + T_{12}|_S^2(\phi_E - \phi_2)) \\ F_E &= -(T_{12}|_E^2(\phi_2 - \phi_S) + T_{22}|_E^2(\phi_E - \phi_2)) = -(T_{12}|_E^3(\phi_3 - \phi_N) + T_{22}|_E^3(\phi_3 - \phi_E)) \\ F_W &= -(T_{12}|_W^1(\phi_S - \phi_1) + T_{22}|_W^1(\phi_W - \phi_1)) = -(T_{12}|_W^4(\phi_N - \phi_4) + T_{22}|_W^4(\phi_4 - \phi_W)) \end{aligned} \tag{14}$$

where, e.g. for the contributing subcell of cell 4 in Figure 2(b), $\phi_\xi = (\phi_N - \phi_4)$. The resulting local linear system of equations is then written as

$$F = A_L\Phi_f + B_L\Phi_v = A_R\Phi_f + B_R\Phi_v \tag{15}$$

where A_L, B_L, A_R and B_R are 4×4 matrices, $F = (F_N, F_S, F_E, F_W)^{\mathrm{T}}$ are the fluxes defined in the dual cell and $\Phi_f = (\phi_N, \phi_S, \phi_E, \phi_W)^{\mathrm{T}}$ are the interface pressures. Similarly, $\Phi_v = (\phi_1, \phi_2, \phi_3, \phi_4)^{\mathrm{T}}$ are the cell-centred pressures. Thus, the four interface pressures are expressed in terms of the four cell-centred pressures. Using Equation (15), Φ_f is now expressed in terms of Φ_v to obtain the dual-cell flux and coefficient matrix

$$F = (A_L(A_L - A_R)^{-1}(B_R - B_L) + B_L)\Phi_v \tag{16}$$

Thus, the cell-face pressures are eliminated from the flux by being determined locally in terms of the cell-centred pressures in a preprocessing step, avoiding introduction of the interface pressure equations into the assembled discretization matrix.

Therefore, flux continuity in the case of a general tensor is obtained while maintaining the standard single degree of freedom per cell. Since the continuity equations depend on both ϕ_ξ and ϕ_η (unless a diagonal tensor is assumed with cell-face mid-point quadrature resulting in a two-point flux), the interface pressures $\Phi_f = (\phi_N, \phi_S, \phi_E, \phi_W)^{\mathrm{T}}$ are locally coupled and each

DOI: 10.1002/fld

group of four interface pressures is determined simultaneously in terms of the group of four cell-centred pressures whose union contains the continuity positions. Finally, for a structured grid the finite-volume scheme is defined by

$$F_{i+1/2,j} - F_{i-1/2,j} + F_{i,j+1/2} - F_{i,j-1/2} = M \tag{17}$$

where i, j are the integer coordinates of the central quadrilateral control volume, cell 1 in Figure 1(a) and

$$\begin{aligned} F_{i+1/2,j} &= F_{S_{i+1/2,j+1/2}} + F_{N_{i+1/2,j-1/2}} \\ F_{i,j+1/2} &= F_{E_{i-1/2,j+1/2}} + F_{W_{i+1/2,j+1/2}} \end{aligned} \tag{18}$$

where $i+\frac{1}{2}$, $j+\frac{1}{2}$ denote the 'integer' coordinates of the top right-hand side dual cell, Figure 1(b). The flux contributions $F_S^+ = F_{S_{i+1/2,j+1/2}}$ and $F_N^- = F_{N_{i+1/2,j-1/2}}$ are illustrated by the arrows in Figure 8, the local pressure support upon which the F_S^+, F_N^- flux approximations are built is indicated by the shaded triangles (which depend on a total of six grid nodes) and the continuity points by squares, Figure 8.

3.1. Loss of symmetry

A symmetric physical-space quadrilateral discretization is only obtained if the physical grid comprised squares, rectangles or parallelograms, where T is spatially constant. For a general quadrilateral cell of arbitrary distortion, the local variation in geometry will mean that the local general-tensor T will vary according to local spatial position in the cell. Referring again to the example subcell in Figure 2(b) in general

$$T_{12}|_W^1 \neq T_{12}|_S^1 \tag{19}$$

which is the source of loss of symmetry in the local subcell flux matrix [6] and consequently loss of symmetry in the global discrete matrix of the *physical*-space formulation. The effect on discretization is discussed below.

3.2. Physical-space flux: inverse tensor form

The flux is now derived in an alternative form involving potential differences between nodes following [4, 5]. We return to the physical-space flux of Equation (14) expressed in terms of potential differences between interface pressures and nodal pressures, for any quadrature point on the interface, and reformulate the flux continuity conditions in terms of the subcell tensors as

$$\begin{aligned} (T^1)^{-1}\begin{pmatrix} F_S \\ F_W \end{pmatrix} &= -\begin{pmatrix} \phi_S - \phi_1 \\ \phi_W - \phi_1 \end{pmatrix}, \quad (T^2)^{-1}\begin{pmatrix} F_S \\ F_E \end{pmatrix} = -\begin{pmatrix} \phi_2 - \phi_S \\ \phi_E - \phi_2 \end{pmatrix} \\ (T^3)^{-1}\begin{pmatrix} F_N \\ F_E \end{pmatrix} &= -\begin{pmatrix} \phi_3 - \phi_N \\ \phi_3 - \phi_E \end{pmatrix}, \quad (T^4)^{-1}\begin{pmatrix} F_N \\ F_W \end{pmatrix} = -\begin{pmatrix} \phi_N - \phi_4 \\ \phi_4 - \phi_W \end{pmatrix} \end{aligned} \tag{20}$$

DOI: 10.1002/fld

where fluxes are grouped according to subcell numbers (denoted by general-tensor superfixes) that are in common, and Equation (20) is then an equivalent form of Equation (14). The physical-space tensor approximations belonging to each subcell are written as

$$T^1=\begin{pmatrix} T_{11}|_S^1 & T_{12}|_S^1 \\ T_{12}|_W^1 & T_{22}|_W^1 \end{pmatrix}, \quad T^2=\begin{pmatrix} T_{11}|_S^2 & T_{12}|_S^2 \\ T_{12}|_E^2 & T_{22}|_E^2 \end{pmatrix}$$
$$T^3=\begin{pmatrix} T_{11}|_N^3 & T_{12}|_N^3 \\ T_{12}|_E^3 & T_{22}|_E^3 \end{pmatrix}, \quad T^4=\begin{pmatrix} T_{11}|_N^4 & T_{12}|_N^4 \\ T_{12}|_W^4 & T_{22}|_W^4 \end{pmatrix} \tag{21}$$

Now denote $T_{12}^1=T_{12}|_S^1$ and $T_{21}^1=T_{12}|_W^1$ then by Equation (19) $T_{12}^1\neq T_{21}^1$ in the general case. Thus, the inverses of the discrete tensors in Equation (21) are not symmetric in the general case. Denoting the inverse of the general tensor by $\widetilde{T}=(T)^{-1}$ and adding pairs of equations operating on common fluxes, e.g. adding the top rows of the first pair of equation sets in Equation (20) yields

$$(\widetilde{T}_{11}^1+\widetilde{T}_{11}^2)F_S+\widetilde{T}_{12}^2F_E+\widetilde{T}_{12}^1F_W=-(\phi_2-\phi_s+\phi_s-\phi_1)=-(\phi_2-\phi_1) \tag{22}$$

which eliminates the unknown interface pressure directly. Gathering the other flux pairs and expanding in a similar fashion lead to a system of equations that expresses the fluxes directly in terms of potential differences, viz

$$A\mathbf{F}=-\Delta\boldsymbol{\phi}_{\mathbf{v}} \tag{23}$$

where

$$\mathbf{F}=(F_S,F_E,F_N,F_W)^{\mathrm{T}}, \quad \Delta\boldsymbol{\phi}_{\mathbf{v}}=(\phi_{21},\phi_{32},\phi_{34},\phi_{41})^{\mathrm{T}} \tag{24}$$

where double suffices of ϕ denote potential differences, e.g. $\phi_{21}=\phi_2-\phi_1$, and the flux coefficient matrix is given by

$$A=\begin{pmatrix} \widetilde{T}_{11}^1+\widetilde{T}_{11}^2 & \widetilde{T}_{12}^2 & 0 & \widetilde{T}_{12}^1 \\ \widetilde{T}_{21}^2 & \widetilde{T}_{22}^2+\widetilde{T}_{22}^3 & \widetilde{T}_{21}^3 & 0 \\ 0 & \widetilde{T}_{12}^3 & \widetilde{T}_{11}^4+\widetilde{T}_{11}^3 & \widetilde{T}_{12}^4 \\ \widetilde{T}_{21}^1 & 0 & \widetilde{T}_{21}^4 & \widetilde{T}_{22}^1+\widetilde{T}_{22}^4 \end{pmatrix} \tag{25}$$

Thus, the dual-cell flux matrix entries are comprised of elements of the general-tensor inverse corresponding to each subcell component of control volume. This form of the physical-space scheme shows the following:

(a) The fluxes can be written as linear combinations of pressure differences around the dual cell, where

$$\mathbf{F}=-A^{-1}\Delta\boldsymbol{\phi}_{\mathbf{v}} \tag{26}$$

which holds for the family of schemes ($0<q\leqslant 1$). Thus, consistency with respect to constant pressure field is demonstrated for any quadrature point q.

(b) The physical-space flux matrix is not generally symmetric.

DOI: 10.1002/fld

(c) The introduction of a symmetric tensor approximation will lead to a symmetric flux matrix and an SPD discrete system [5], also see Sections 5 and 6.
(d) The connection between the physical-space scheme and the MFE method can be made, cf. Section 8.

The fluxes of Equation (23) embody the full tensor generalization of the harmonic mean. This is seen by considering the case of a diagonal tensor with $q=1$. In this case at each interface, Equation (23) reduces to

$$-\frac{1}{2}\left(\frac{h}{K_{\mathrm{r}}}+\frac{h}{K_{\mathrm{l}}}\right)F=(\phi_{\mathrm{r}}-\phi_{\mathrm{l}}) \tag{27}$$

where for a given interface, l and r denote the respective left- and right-hand side control volumes. Rearranging Equation (27) leads directly to the well-known two-point flux approximation with harmonic mean coefficient.

For the base scheme $q=1$, the positions of interface pressures from adjacent dual cells will coincide. While each interface pressure is continuous in the direction normal to the control-volume face by construction, the interface pressures can be discontinuous in the tangential direction (to the interface), i.e. between adjacent dual cells when a full tensor is present. This crucial step leads to the system being locally coupled. Conversely, had the interface pressures been continuous tangentially as well as in the normal direction, the system would be globally coupled. We will return to this point during the discussion of the connection with the mixed method in Section 8.

4. POSITIVE-DEFINITE PHYSICAL-SPACE q-FAMILY

A (not necessarily symmetric) matrix M_G is positive definite if for any non-zero vector $\mathbf{\Phi}_G$

$$\mathbf{\Phi}_G^{\mathrm{T}} M_G \mathbf{\Phi}_G > 0 \tag{28}$$

Following [3, 5], the scalar product of Equation (28) is calculated as a sum of dual cell (dual of the control volume) contributions with

$$\mathbf{\Phi}_G^{\mathrm{T}} M_G \mathbf{\Phi}_G = \sum_{i_{\mathrm{DC}}} \mathbf{\Phi}_v^{\mathrm{T}} M_{i_{\mathrm{DC}}} \mathbf{\Phi}_v \tag{29}$$

where i_{DC} indexes a dual cell. Thus, Equation (28) holds true if the dual-cell energy is positive with

$$\mathbf{\Phi}_v^{\mathrm{T}} M_{i_{\mathrm{DC}}} \mathbf{\Phi}_v > 0 \tag{30}$$

for all dual cells. Expanding the dual-cell inner product

$$\begin{aligned}\mathbf{\Phi}_v^{\mathrm{T}} M_{i_{\mathrm{DC}}} \mathbf{\Phi}_v &= \phi_1(F_S+F_W)+\phi_2(-F_S+F_E)-\phi_3(F_E+F_N)+\phi_4(-F_W+F_N)\\ &= -(F_S\phi_{21}+F_E\phi_{32}+F_N\phi_{34}+F_W\phi_{41})\end{aligned} \tag{31}$$

Using the continuity conditions of Equation (14) where, e.g. at S the left and right fluxes are

$$\begin{aligned}F_S = F_S^1 &= -(T_{11}|_S^1(\phi_S-\phi_1)+T_{12}|_S^1(\phi_W-\phi_1))\\ F_S = F_S^2 &= -(T_{11}|_S^2(\phi_2-\phi_S)+T_{12}|_S^2(\phi_E-\phi_2))\end{aligned} \tag{32}$$

DOI: 10.1002/fld

and similarly $F_W = F_W^1 = -(T_{12}|_W^1(\phi_S - \phi_1) + T_{22}|_W^1(\phi_W - \phi_1))$, we rearrange Equation (31) by using identities of the form

$$-F_S\phi_{21} = -F_S(\phi_2 - \phi_S + \phi_S - \phi_1) = -F_S^2(\phi_2 - \phi_S) - F_S^1(\phi_S - \phi_1) \tag{33}$$

together with similar identities for the other terms of Equation (31) so that the dual-cell energy inner product takes the form

$$\mathbf{\Phi}_v^{\mathrm{T}} M \mathbf{\Phi}_v = (F_S^1\phi_{1S} + F_S^2\phi_{S2} + F_E^2\phi_{2E} + F_E^3\phi_{E3} + F_N^4\phi_{4N} + F_N^3\phi_{N3} + F_W^4\phi_{W4} + F_W^1\phi_{1W}) \tag{34}$$

where again, double suffices of ϕ notate potential differences, e.g. $\phi_{1S} = \phi_1 - \phi_S$. Gathering terms common to each local control-volume subcell, then, e.g. for local control-volume 1 using Equations (32) and (34) yields

$$F_S^1\phi_{1S} + F_W^1\phi_{1W} = T_{11}^1\phi_{S1}^2 + 2\overline{T}_{12}\phi_{S1}\phi_{W1} + T_{22}^1\phi_{W1}^2 \tag{35}$$

where the average cross term is defined by

$$\overline{T}_{12} = \frac{(T_{12}^1 + T_{21}^1)}{2} \tag{36}$$

Provided the local discrete tensor is elliptic with

$$\overline{T}_{12}^2 \leqslant (T_{11}^1 T_{22}^1) \tag{37}$$

the quadratic (in potential differences ϕ_{S1}, ϕ_{W1}) of Equation (35) has at most one root so that

$$F_S^1\phi_{1S} + F_W^1\phi_{1W} \geqslant 0 \tag{38}$$

The other subcell energy contributions are also non-negative provided that the corresponding subcell tensor approximations are elliptic with respect to the respective local mean cross terms. The Dirichlet condition ensures strictly positive energy and consequently a positive-definite system is obtained. The above analysis shows that the schemes are positive definite if the symmetric part of the local discrete tensor $\mathbf{T}$, i.e. $\frac{1}{2}(\mathbf{T} + \mathbf{T}^{\mathrm{t}})$ (superfix t is transpose) is positive-definite over each subcell. Recall that in general, $\mathbf{T} = \mathbf{T}(q)$, the positive-definite property is tested for a range of q for the cases presented in the results section.

Note that this result does not require that the tensor actually be symmetric and, therefore, applies for all quadrature points q and, thus, the whole family of both physical-space and transform-space schemes provided that Equation (37) holds for each subcell energy contribution. An SPD scheme will result if each discrete subcell tensor is symmetric ($T_{12}^i = T_{21}^i$) and elliptic $T_{12}^{i2} \leqslant (T_{11}^i T_{22}^i)$, as constructed in the next sections. The SPD result will then follow from the above since the flux matrix Equation (25) will then be symmetric, leading to a symmetric global matrix [5] and ellipticity ensures that Equation (29) is positive. These results also hold for triangles, the cell vertex formulation is treated in [5] and cell-centred formulation in [32].

5. SYMMETRIC POSITIVE-DEFINITE TENSOR APPROXIMATION

Loss of symmetry in the general tensor occurs in the physical-space approximation due to the variation in general tensor over the control-volume faces, as discussed in the above section. A SPD

DOI: 10.1002/fld

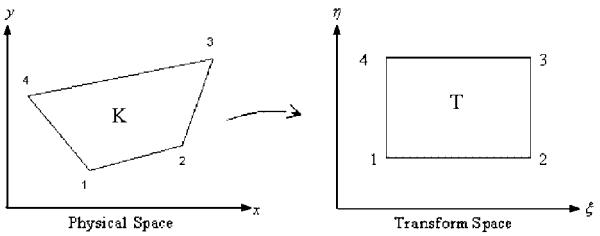

Figure 4. Control-volume cell-wise transformation.

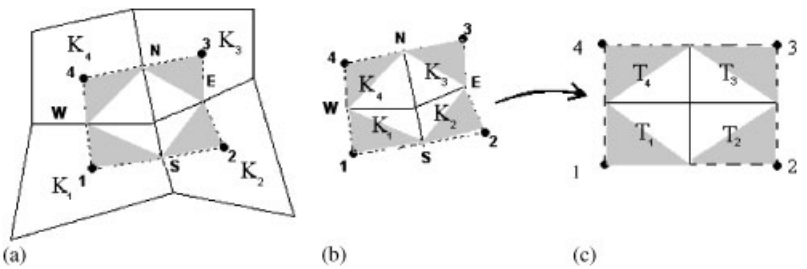

Figure 5. (a) Physical-space quads and piecewise constant tensor (*quadrature point* $q=1$); (b) piecewise constant tensor over subcells; and (c) subcell transformation to piecewise constant general tensor per subcell.

formulation is favoured theoretically for proving convergence and practically for using simpler more robust solvers.

The first flux-continuous schemes that have been shown to be SPD for quadrilateral meshes were obtained by using a *transform*-space formulation at the cell level where a mean piecewise constant general-tensor approximation is used over each cell (or control volume), Figure 4, and the general tensor is approximated at the cell centre [3, 10].

More general and improved SPD formulations are presented in [6, 7]. These schemes are motivated by the result in [5], where it is proven that an SPD flux-continuous scheme is obtained for $q=1$ if each pair of subcell fluxes is defined with respect to a *single* piecewise constant *symmetric elliptic* general tensor per subcell, Figure 5, where local numbering refers to the subcells of the control volume. The actual definitions of the approximate tensor considered here are given in the subsections below. These approximations have been shown to lead to a symmetric flux matrix and a SPD discretization matrix [5] as discussed in the previous section. A SPD discrete general tensor is a fundamental condition for obtaining a symmetric positive discrete matrix. Also construction of a *unique* local SPD tensor within the definition of the local subcell flux approximation mirrors the analytical SPD flux property.

While both formulations (cell level and subcell level) ensure that the discrete matrix is SPD for $q=1$, the subcell formulation first proposed by Edwards [5–7] has important advantages over the cell-wise *transform*-space formulation proposed in [3, 10]. By definition a piecewise constant subcell tensor is a superior approximation of the tensor since it allows a finer-scale variation in the tensor geometry, precisely on the sub-scale, resulting in four discrete values compared with a single value at the cell level, for a given quadrilateral cell. This has important convergence implications

DOI: 10.1002/fld

and the practical outcome in terms of convergence rates is presented in the results section. Secondly, unlike the cell-wise approximation, the subcell scheme generalizes to unstructured grids as in [5–7], allowing any grid combination of quadrilateral and/or triangular cells. In all cases, the subcell flux-continuous schemes are SPD for any grid type, for $q=1$, provided the subcell tensor is SPD.

However, SPD formulations are obtained at the expense of an additional approximation in geometry, compared with the physical-space formulation which maintains exact geometry and is therefore more accurate. Also as shown in Section 4, the non-symmetric physical-space formulation can still retain a positive-definite discrete matrix subject to Equation (37).

One of the key issues in constructing an SPD formulation is the identification of the appropriate local approximation of general-tensor T^k, for each subcell $k=(1,\ldots,4)$.

In principle, there are an infinite number of possibilities depending upon the point chosen to evaluate the tensor inside the subcell. In each of the following subcell tensor approximations, the new local piecewise constant tensors T restore symmetry and ellipticity, e.g. instead of Equation (19) we now have

$$\mathsf{T}_{12}|_W^1=\mathsf{T}_{12}|_S^1=\mathsf{T}_{12}|^1 \tag{39}$$

Different possible general-tensor approximations have already been presented for triangles and quadrilaterals in [6, 7]. Here, we consider three of the many possible approximations for quadrilateral grids.

5.1. *Positive definite—simple average*

The first definition, motivated by Section 4, is defined by a simple average of the cross terms, for example, with respect to subcell 1

$$\mathsf{T}_{12}|^1=\tfrac{1}{2}(T_{12}|_W^1+T_{12}|_S^1) \tag{40}$$

this has the effect of replacing the local tensor T^j by

$$\tfrac{1}{2}(T^j+(T^j)^t) \tag{41}$$

(where superfix t denotes transpose) which is one of a number of approximations motivated by Equation (36) and the general definition of a positive-definite matrix (i.e. $\frac{1}{2}(A^j+(A^j)^t)$) when the matrix is non-symmetric. While Equation (40) symmetrizes the tensor for any quadrature q, by experiment, convergence is found to be at best poor.

5.2. *Local subcell mapping and subcell centre tensor*

The second definition [6, 7], is a local mean general tensor, for each local sub-quadrilateral of every primal quadrilateral cell. In this case each sub-quadrilateral is in effect mapped to a unit cell *via* a bilinear transformation given as

$$\mathbf{r}=\mathbf{r}_1(1-\xi)(1-\eta)+\mathbf{r}_A\xi(1-\eta)+\mathbf{r}_{V3}\xi\eta+\mathbf{r}_B(1-\xi)\eta \tag{42}$$

where $\mathbf{r}$ is the position vector of an arbitrary point in the subcell, $\mathbf{r}_i$ $(i=1, A, V3, B)$, are the position vectors of the subcell corner coordinates and $0\leqslant(\xi,\eta)\leqslant 1$ are the local unit transformed subcell coordinates as illustrated in Figure 6(a). The tensor can be defined at any point in or on

DOI: 10.1002/fld

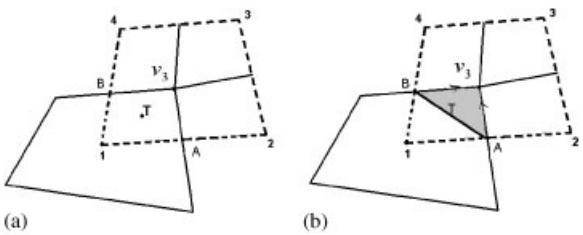

Figure 6. (a) Control-volume subcell centre tensor ($\xi=0.5, \eta=0.5$) and (b) control-volume subcell face tensor ($\xi=1, \eta=1$) on shaded triangle. *Quadrilateral primal grid cell* (*solid line*) *dual cell* (*dashed line*), *subcell* ($1, A, V3, B$). Subcell transform coordinate system origin ($\xi=\eta=0$) corresponds to primal grid quadrilateral mid-point 1.

the quadrilateral *via* the coordinates (ξ, η), leading to an infinite choice. In the second definition [6] we choose ($\xi=0.5, \eta=0.5$) corresponding to the mean subcell centre value.

5.3. Control-volume face tensor

In the third definition following [6, 7], the piecewise constant tensor is defined with respect to the subcell control-volume face geometry, Figure 6(b). The local general tensor is built in a coordinate system directly aligned with the two control-volume faces, so that the surface normal vectors are naturally incorporated within the formulation. This formulation is most closely associated with the physical-space control-volume sub-faces and the approximation corresponds to ($\xi=1, \eta=1$), Equation (42). Thus, the tensor is defined by the geometry of the triangle ($B, A, V3$) defined by the two parent control-volume *sub-faces*, i.e. the two faces of the subcell as indicated in Figure 6(b) by the two arrow heads. In contrast, the $q=1$ pressure sub-triangle is defined by $(A, B, 1)$. The tensor approximation is robust provided that no pair of control-volume subcell faces are parallel. If parallel sub-faces are detected the previous subcell centre tensor approximation is used.

It is anticipated that this approximation will be the most successful, since by definition it is based entirely on control-volume face geometry.

6. FAMILY OF SUBCELL SPACE SCHEMES AND SYMMETRIC POSITIVE-DEFINITE APPROXIMATION

The family of subcell space tensor schemes is readily defined by returning to Section 3 and replacing the physical-space tensors of Equation (21) with the piecewise constant SPD subcell tensors T defined in the previous section, where

$$\mathsf{T}^i = \begin{pmatrix} \mathsf{T}_{11}|^i & \mathsf{T}_{12}|^i \\ \mathsf{T}_{12}|^i & \mathsf{T}_{22}|^i \end{pmatrix}, \quad i=1,\ldots,4 \tag{43}$$

and the tensor superfix corresponds to the local number of the subcell in the dual cell. The subcell schemes follow directly, using Equation (43) in Equations (12)–(16) now formed with respect to each local subcell transform space where

$$\phi_\xi = J(\phi, \eta)/J(\xi, \eta), \quad \phi_\eta = J(\xi, \phi)/J(\xi, \eta) \tag{44}$$

DOI: 10.1002/fld

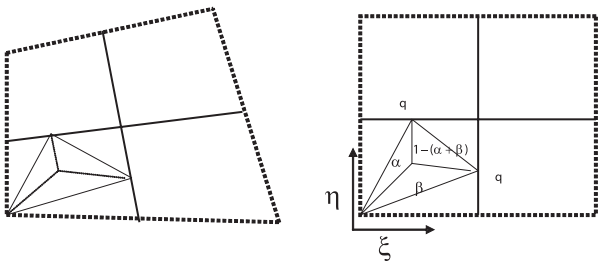

Figure 7. Subcell transform space and general quadrature point q.

where $J(\xi,\eta)=\xi_\alpha\eta_\beta-\xi_\beta\eta_\alpha$, and (α,β) are area coordinates of the pressure sub-triangle in subcell transform space, Figure 7. The range of quadrature points corresponds to the interface pressure points as before and now define a family of schemes in subcell transform space.

6.1. Subcell tensor SPD flux

In [5] it is shown that the base member of the family of subcell transform-space schemes (quadrature $q=1$) yields a SPD discretization matrix for quadrilateral and triangle meshes. The base (SPD) scheme flux is derived directly below in cell-centred form. Using (one-sided) control-volume face mid-point quadrature ($q=1$) (Figure 5) and repeating the steps of Equations (20)–(25) with Equation (21) replaced by Equation (43) with a piecewise constant symmetric tensor per subcell, the subcell flux vector corresponding to the dual cell is given by

$$A\mathbf{F}=-\Delta\boldsymbol{\phi}_{\mathbf{v}} \tag{45}$$

where

$$\mathbf{F}=(F_S,F_E,F_N,F_W)^{\mathrm{T}},\quad \Delta\boldsymbol{\phi}_{\mathbf{v}}=(\phi_{21},\phi_{32},\phi_{34},\phi_{41})^{\mathrm{T}} \tag{46}$$

and in this case the flux coefficient matrix is *symmetric*, with

$$A=\begin{pmatrix} \widetilde{\mathsf{T}}^1_{11}+\widetilde{\mathsf{T}}^2_{11} & \widetilde{\mathsf{T}}^2_{12} & 0 & \widetilde{\mathsf{T}}^1_{12} \\ \widetilde{\mathsf{T}}^2_{12} & \widetilde{\mathsf{T}}^2_{22}+\widetilde{\mathsf{T}}^3_{22} & \widetilde{\mathsf{T}}^3_{12} & 0 \\ 0 & \widetilde{\mathsf{T}}^3_{12} & \widetilde{\mathsf{T}}^4_{11}+\widetilde{\mathsf{T}}^3_{11} & \widetilde{\mathsf{T}}^4_{12} \\ \widetilde{\mathsf{T}}^1_{12} & 0 & \widetilde{\mathsf{T}}^4_{12} & \widetilde{\mathsf{T}}^1_{22}+\widetilde{\mathsf{T}}^4_{22} \end{pmatrix} \tag{47}$$

where $\widetilde{\mathsf{T}}=\mathsf{T}^{-1}$. The dual-cell flux matrix entries are now comprised of elements of the inverse of the subcell tensors corresponding to each subcell component of control volume within the dual cell. Symmetry of the flux matrix Equation (47) follows from symmetry of the subcell tensors. In contrast, compare the physical-space flux matrix of Equation (25) with the subcell tensor flux matrix Equation (47). Symmetry of the flux matrix Equation (47) leads to a symmetric discretization matrix together with positive definiteness, cf. Section 4 and [5]. We note that while the physical-space schemes (for all q) and transform-space schemes with $q\neq 1$ are not generally symmetric, the systems are positive definite if Equation (37) holds.

DOI: 10.1002/fld

The subcell fluxes of Equations (23), (45) embody the full tensor generalization of the harmonic mean. If the tensor is locally diagonal and $q=1$ the interface equations reduce to the form of Equation (27) or

$$F=-\frac{2K_{\mathrm{l}}K_{\mathrm{r}}(\phi_{\mathrm{r}}-\phi_{\mathrm{l}})}{h(K_{\mathrm{l}}+K_{\mathrm{r}})} \tag{48}$$

recovering the well-known two-point flux approximation with harmonic mean coefficient.

7. RELATIONSHIP WITH THE MIXED FINITE ELEMENT METHOD

Following on from the above formulation, the relationship between these schemes and the MFE method is presented in this section. For diagonal tensors with two-point flux see [19] and for full tensors the relationship is given in [5]. The relationship between the above schemes and that of the mixed method is fundamental and is extended here to both *physical-space* and *subcell transform-space* for all q (*cellwise transform space* follows the same path). Russel and Wheeler [19] have shown that the standard diagonal tensor scheme with harmonic mean coefficients is equivalent to the lowest order mixed method with special quadrature.

For full tensors the relationship is derived in a simple and direct way, by extending the observation of Russel and Wheeler in 1983. The key to unlocking the relationship for the general full tensor case follows [5] and the path is given below.

7.1. CVD(MPFA)

(1) *CVD*(*MPFA*) *physical space*: The *physical-space* (CVD-MPFA) schemes are derived with respect to the physical-space inverse general-tensor $\tilde{T}$ following Equations (20)–(26) above for any q, where in the general case these schemes do not have symmetric matrices, but are conditionally positive definite, cf. Section 4.

(2) *CVD*(*MPFA*) *subcell transform space*: The *subcell transform-space* CVD(MPFA) schemes are derived with respect to the subcell transform-space inverse general-tensor $\tilde{\mathsf{T}}$, following Equations (43)–(47), with T locally piecewise constant over each subcell, (one-sided) $q=1$ quadrature ensures that the matrix is SPD. (Note that for subcell schemes, when $(0<q<1)$ and $q\neq 1$ the transform causes a loss in symmetry in the general case, though again the schemes are conditionally positive definite, cf. Section 4.)

7.2. The mixed finite element method

The mixed method [18] is derived by representing the second-order partial differential equation in Equation (1) as two first-order partial differential equations

$$\begin{aligned} -\mathbf{K}^{-1}V &= \nabla\phi \\ \nabla\cdot V &= q \end{aligned} \tag{49}$$

where q is a source term and seeking the solution (V,ϕ) of the weak variational form

$$\begin{aligned} -(\mathbf{K}^{-1}V,\mathbf{v}) &= (\nabla\phi,\mathbf{v}) \\ (\nabla\cdot V,w) &= (q,w) \end{aligned} \tag{50}$$

DOI: 10.1002/fld

where $(\mathbf{v}, w)$ are appropriate test functions. The solution (V, ϕ) and test functions $(\mathbf{v}, w)$ are in $H(\mathrm{div}) \times L_2$, where

$$H(\mathrm{div}) = \{\mathbf{v} \in (L_2)^2 : \nabla \cdot \mathbf{v} \in L_2\} \tag{51}$$

and $q \in L_2$. The mixed method considered here is initially standard, constructed using the lowest order Raviart–Thomas elements and employs tensor products of $(\mathbf{v}, w)$ with w piecewise constant and $\mathbf{v} = (v_x, v_y)$ piecewise linear. Since w is piecewise constant the second inner product of Equation (50) is simply the integral of divergence which is readily identified in the above formulation. For the full tensor case, the first inner product of Equation (50) requires special treatment as presented in [5]. This is motivated by the crucial observation of Russel and Wheeler [19], which involves identifying the approximate diagonal tensor two-point flux as a special version of the weak form of the first inner product in Equation (50). In particular, it is shown in [19] that the standard diagonal tensor scheme with harmonic mean coefficients is equivalent to the lowest order mixed method with trapezoidal quadrature in x (across the interface) and mid-point rule in y (tangential to the interface). Their key observation is given below for the first inner product approximation at the right-hand control-volume face $(i+\frac{1}{2}, j)$ of a Cartesian cell (i, j) with

$$\begin{aligned}\left(\frac{1}{K}U_x, v^x_{i+1/2} w^y_j\right)_{T_x M_y} &= \frac{\Delta x}{2}\left(\frac{1}{K_{i,j}} + \frac{1}{K_{i+1,j}}\right)(U_x)_{i+1/2,j} \\ &= -(\phi_{i+1,j} - \phi_{i,j})\end{aligned} \tag{52}$$

where U_x is the x component of velocity and suffices T_x, M_y, denote the trapezoidal and mid-point quadrature rules in x and y directions, respectively (where x is normal and y is tangential to the control-volume face) and let $v^x_{i+1/2}$, w^y_j denote the respective linear and piecewise constant basis functions, cf. [19].

For a full tensor flux, the above observation requires a modification as presented in [5] and is given here together with an extension. In addition to the SPD base case $q = 1$ treated in [5], it is shown that both the physical-space and transform-space *families* of schemes can also be identified as special mixed methods, for all quadrature points.

While the relationship between Equations (22)–(26) and Equation (52) is clear for the diagonal tensor case, if the mid-point rule (M_y) is used for the full tensor case the system is fully coupled with global fluxes. In this case the fluxes and pressures are coupled primary variables of the system. Instead of the mid-point rule, we use one-sided integration over one half of each control-volume face belonging to a dual cell, cf. Section 3, so that upon assembly of all dual-cell contributions, the mid-point rule is split (along the tangential direction to each control-volume face) into two halves enabling the locally coupled system of Equations (22)–(26) with respect to the physical space tensor T (or Equations (45)–(47) with respect to the subcell transform space tensor T) to be recovered. The modified integration rule for the right-hand face of the central cell (i, j) of Figure 8 (i.e. cell 1 in Figure 1), is defined by two half-face approximations, the upper half is expressed as

$$\begin{aligned}(\mathbf{T}^{-1} F|_S, v^\xi w^\eta)_{T_\xi M^+_\eta} &= (\tilde{T}^1_{11} + \tilde{T}^2_{11}) F_S + \tilde{T}^2_{12} F_E + \tilde{T}^1_{12} F_W \\ &= -(\phi_2 - \phi_1)\end{aligned} \tag{53}$$

DOI: 10.1002/fld

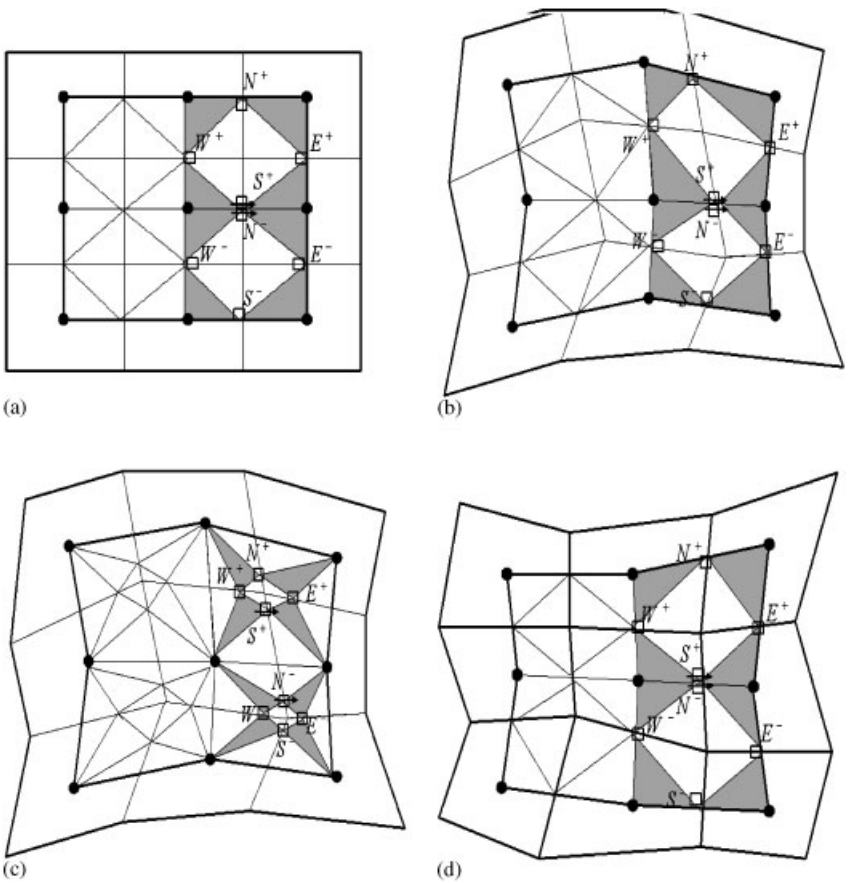

Figure 8. (a) Subcell transform space $q=1$; (b) subcell physical-space $q=1$; (c) physical-space general quadrature point q; and (d) distorted transform-space $q=1$.

where suffix M_η^+ indicates one-sided integration over the upper subcell face in the tangential η^+ direction leading to an equation for F_S^+. A similar trapezoidal rule (across the face) and tangential subcell integration is applied to the other control-volume subfaces, Figure 8. Relative to node i, j the net control-volume face flux at face $i+\frac{1}{2}, j$ cf. Equation (18), is comprised of $F_S^+ + F_N^-$. The upper sub-face flux $F_S^+ = F_{S_{i+1/2,j+1/2}}$ is derived from the upper contributing $i+\frac{1}{2}, j+\frac{1}{2}$ dual-cell equation set, where Equation (53) is one of the four (one-sided) integrations. Similarly, a lower sub-face flux $F_N^- = F_{N_{i+1/2,j-1/2}}$ is derived from the lower contributing $i+\frac{1}{2}, j-\frac{1}{2}$ dual-cell equation set, where

$$(\mathbf{T}^{-1}F|_N, v^\xi w^\eta)_{T_\xi M_\eta^-} = \tilde{T}_{12}^3 F_E + (\tilde{T}_{11}^4 + \tilde{T}_{11}^3) F_N + \tilde{T}_{12}^4 F_W$$
$$= -(\phi_2 - \phi_1) \tag{54}$$

where suffix M_η^- indicates one-sided integration over the lower subcell face in the tangential η^- direction, Equation (54) is one of the four integrations in dual cell $i+\frac{1}{2}, j-\frac{1}{2}$.

DOI: 10.1002/fld

This observation shows the underlying relationship between the finite volume methods proposed above and the mixed method for full tensor fluxes. In effect the above definition of the split quadrature rule, applied tangentially to each control-volume face, introduces a split Raviart–Thomas representation of velocity–pressure over each half cell. This in turn implies that the proof of convergence of the schemes presented here relates directly to that of the mixed method.

For the $q=1$ SPD scheme in subcell transform space, with T piecewise constant per subcell (replace T with T in Equations (53) and (54)), the subcell transform-space fluxes F_S^+, F_N^- are represented in Figure 8(a) by the arrows in the (flux-pressure continuity points) squares, the corresponding linear pressure support is indicated by the shaded triangles. (While the $q=1$ cell-wise transform-space scheme is also SPD and relates to the mixed method through the same path, the cell-wise scheme is specialized to quadrilateral grids and is less accurate than the subcell scheme for variable geometry, as shown in the results section.)

For the physical-space schemes the $q=1$ fluxes F_S^+, F_N^- are indicated in Figure 8(b); see arrows, and the general q-fluxes F_S^+, F_N^- are in Figure 8(c) (see arrows). While the tensor is non-symmetric in the general case, the schemes are positive definite if Equation (37) holds. The relationships between Equations (53) and (54)) and Equations (22)–(26) hold for all q $(0<q\leqslant 1)$, with MFE applied to a non-symmetric tensor field that is a local function of q, Figure 8(c). While the general q-fluxes (F_S^+, F_N^-) in physical space rely on the support shown in Figure 8(c), the relationship with MFE can still be derived, since Equation (14) can be reinterpreted as a $q=1$ scheme in another *distorted* transform space Figure 8(d), which reflects the non-symmetry of the local tensor in the general case. The usual Trapezoidal half-cell face (onesided) integration rule is now applied in the *distorted* space.

In summary, the main difference is in the treatment of the discontinuous pressure gradient. The above finite-volume methods introduce temporary auxiliary interface pressures that enable subcell pressure gradients and consequently fluxes and flux continuity conditions to be defined locally in the dual cells with no global coupling. Alternatively, we can use the mixed method where the weak form of the pressure gradient is used. By modifying the integration rule of [19], the full tensors are treated by replacing the mid-point rule with a simple one-sided integration rule (per half control-volume face) that circumvents the global coupling of the interface pressures and enables the algebraic system of Section 3 to be derived.

Thus, the key is to break the mid-point rule in the Russel and Wheeler trapezoidal-mid-point quadrature and apply 'one-sided' integration or quadrature over one half of each control-volume face with a quadrature rule that matches the above CVD schemes. This crucial step splits the mid-point quadrature rule (in the Russel and Wheeler analysis) and breaks the global coupling [5] as pressure is only continuous in the normal direction as discussed in Section 3. Equations (14)–(25) are then traced backwards to recover the physical-space CVD(MPFA) schemes. Equations (43)–(47) are traced backwards to recover the subcell transform-space CVD(MPFA) schemes.

8. MONOTONICITY

The general conditions for these schemes to have an M-matrix were first derived in [2, 3] and are stated below

$$|T_{12}|\leqslant \eta(T_{11}+T_{22})\leqslant \min(T_{11}, T_{22}) \tag{55}$$

DOI: 10.1002/fld

where η is a function of a quadrature point. A detailed study of the implications of this result for various quadratures will be presented in a future paper [33]. Extension to double families is presented in [31]. Here, we note that the two inequalities lead to different schemes. For example, choosing η to satisfy the left inequality with

$$\eta = |T_{12}|/(T_{11}+T_{22}) \tag{56}$$

yields a seven-point (diagonally orientated) scheme when T_{12} is of fixed sign, which can improve monotonicity. Choosing η to satisfy the right-hand inequality with

$$\eta = \min(T_{11}, T_{22})|/(T_{11}+T_{22}) \tag{57}$$

yields a seven-point 'H'-shape support scheme if $T_{22} = \min(T_{11}, T_{22})$, or a seven-point '$I$'-shape support scheme if $T_{11} = \min(T_{11}, T_{22})$. Substituting η defined by Equation (56) or Equation (57) into Equation (55) shows that the schemes have M-matrices if

$$|T_{12}| \leqslant \min(T_{11}, T_{22}) \tag{58}$$

which is a sufficient condition for ellipticity, but not necessary, therefore M-matrices only result for a limited range of possible full elliptic tensors. If η is defined by Equation (57), then for large ratios, e.g. $T_{11} \gg T_{22}$ caused by large grid aspect ratio or permeability ratio, η will tend to zero, so that the base scheme ($q = 1$) will be selected as a limiting case. Further details are given in [33].

9. NUMERICAL RESULTS

In this section, we present a study of the effect of both subcell tensor approximation, where the tensor is calculated using control-volume face geometry (Figure 4) and quadrature point on convergence of the subcell scheme formulation. A comparison is made between the subcell formulation, physical-space formulation and the cell-wise transformed control-volume scheme. A positive-definite test of the physical space and subcell transform-space tensors is also conducted for each q considered in the convergence study (except for subcell transform space $q = 1$, which is SPD). For all grids, the discrete physical-space and subcell transform-space tensors are found to be positive definite for $q = 0.5$ and 1.

9.1. Convergence results

A convergence study and comparison between schemes are presented using the range of quadrature points $q = 0.1, 0.5$ and 1. We note that the numerical convergence study of the family of flux-continuous schemes in *physical* space has shown that quadrature point $q = 0.1$ yields improved convergence when compared with other quadrature points [8]. The schemes presented here are tested on the grids shown in Figure 9.

Pressure and velocity convergence are measured using the L_2-error *norm* (*versus* $\sqrt{\text{no. of control} - \text{volumes}}$) where

$$L_2 = \left(\frac{\sum_i (A_i (p_i^{\text{analytical}} - p_i^{\text{numerical}})^2)}{\sum_i A_i} \right)^{1/2} \tag{59}$$

DOI: 10.1002/fld

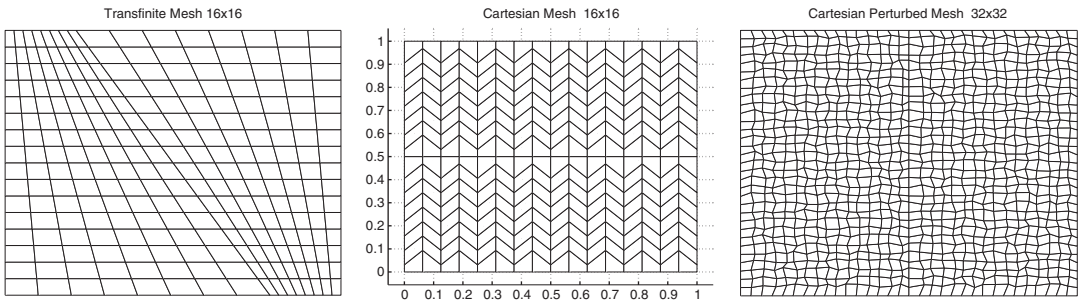

Figure 9. (a) Transfinite mesh aligned along $\theta = 2\pi/3$ discontinuity; (b) zig-zag grid honouring internal discontinuity along X and Y axes; and (c) Cartesian perturbed grid honouring discontinuity.

and A_i is the area of the grid cell i. The grid refinement levels used for the L_2 *norm* calculation are 8×8, 16×16, 32×32 and 64×64 for all test cases. In each case, the analytical solution is used to define Dirichlet boundary conditions.

Case 1: The first test example involves uniform flow over a rectangular domain with a diagonal permeability tensor $\mathbf{K} = c\mathbf{I}$, where $c = 10$. The exact pressure field is linear and is defined by

$$\phi(x, y) = x + y - \tfrac{1}{2} \tag{60}$$

The exact solution is used to define the Dirichlet boundary conditions of the equivalent numerical problem. The numerical solution corresponding to Equation (60) is obtained on a quadrilateral grid aligned with the exterior boundary and an interior boundary oriented at $2\pi/3$ from the horizontal line as shown in Figure 9(a). The numerical pressure and velocity are found to be exact for all quadrature points when using the *physical*-space scheme as control-volume geometry is exactly represented and the numerical approximation and exact solution are both piecewise linear. Since the tensor fields are found to be positive definite for this case (so that discrete operator M_G is positive definite and the inverse exists) the exact solution property can be deduced from the discrete error equation $M_G e_h = 0$, where solution error $e_h = \phi(x, y) - \phi_h$ (difference between exact and discrete solutions).

For the cell-wise transform-space scheme, convergence of the numerical solution is found to be of the order h^2 for pressure and velocity [3, 8, 9].

On solving the problem with the subcell scheme, numerical convergence of pressure and velocity is found to be of order slightly greater than h^2 for all quadrature points. The errors obtained in numerical pressure and velocity are found to be much less when using the subcell formulation (Figure 10(b)) compared with the cell-wise formulation (Figure 10(a)). This is consistent with using the superior tensor approximation provided by the subcell scheme.

Case 2: The next test also involves a homogeneous medium with diagonal permeability tensor, given by $\mathbf{K} = c\mathbf{I}$, where $c = 1000$. The reference solution is smooth with analytical pressure field given by

$$\phi(x, y) = \sin(\pi x)\sinh(\pi y) \tag{61}$$

Dirichlet boundary conditions are applied on the boundary of a square domain with a grid similar to the previous example. The order of convergence of pressure and velocity is found to be close

DOI: 10.1002/fld

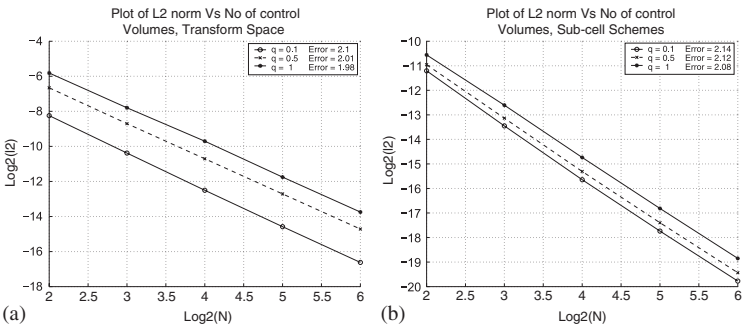

Figure 10. Case 1: (a) plot of L_2 error norm for pressure, cell-wise transform space and (b) plot of L_2 error norm for pressure, subcell scheme.

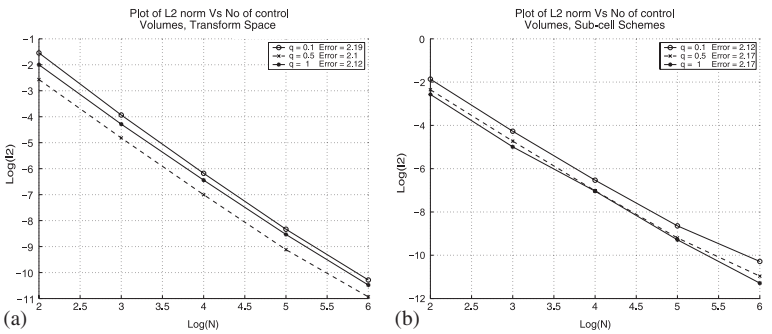

Figure 11. Case 2: (a) L_2 error norm of pressure error using cell-wise transform space and (b) L_2 error norm of pressure error using subcell space scheme.

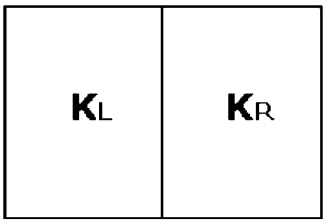

Figure 12. Case 2: discontinuous tensor field.

to h^2 for the cell-wise control-volume formulation. Whereas for the subcell scheme formulation the order of convergence for pressure and velocity is found to be h^2 for all quadrature points. As in the previous test case error magnitudes are found to be less for the subcell scheme formulation for all quadrature points compared with the cell-wise formulation, see Figure 11.

Case 3: The third example involves a discontinuous jump in permeability and is therefore more challenging than the previous examples. The solution [3] is included below Equation (62) for completeness. The domain shown in Figure 12 has a permeability discontinuity at $x = 0.5$ and the

DOI: 10.1002/fld

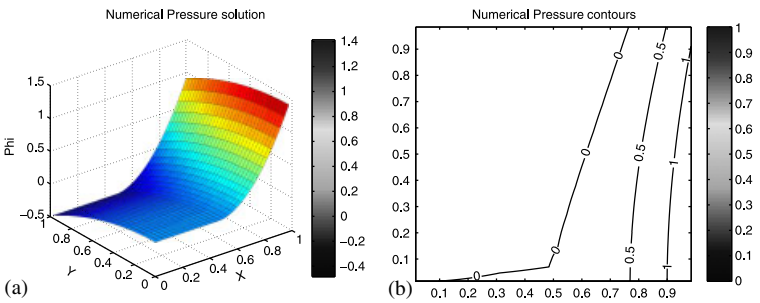

Figure 13. Case 3: (a) numerical pressure solution using subcell scheme and (b) numerical pressure contours.

permeability tensor is quite distinct in the two sub-domains.

$$
\begin{aligned}
\phi(x,y) &= \begin{cases} c_{\mathrm{l}}x^2+d_{\mathrm{l}}y^2, & x<\frac{1}{2} \\ a_{\mathrm{r}}+b_{\mathrm{r}}x+c_{\mathrm{r}}x^2+d_{\mathrm{r}}y^2, & x\geqslant\frac{1}{2} \end{cases} \\
K &= \begin{cases} \begin{pmatrix} 50 & 0 \\ 0 & 1 \end{pmatrix}, & x<\frac{1}{2} \\ \begin{pmatrix} 1 & 0 \\ 0 & 10 \end{pmatrix}, & x\geqslant\frac{1}{2} \end{cases} \\
\alpha &= K_{11}|_{\mathrm{r}}/K_{11}|_{\mathrm{l}} \\
\beta &= K_{22}|_{\mathrm{l}}/K_{22}|_{\mathrm{l}} \\
a_{\mathrm{r}} &= 1 \\
f &= 4a_{\mathrm{r}}/((\alpha-2)\beta+1) \\
b_{\mathrm{r}} &= (\beta-1)f \\
c_{\mathrm{r}} &= f \\
d_{\mathrm{r}} &= -c_{\mathrm{r}}K_{11}|_{\mathrm{r}}/K_{22}|_{\mathrm{r}} \\
c_{\mathrm{l}} &= \alpha\beta c_{\mathrm{r}} \\
d_{\mathrm{l}} &= d_{\mathrm{r}}
\end{aligned}
\tag{62}
$$

The above numerical example has been tested previously [3, 8] and $O(h^2)$ convergence for pressure and close to $O(h^2)$ convergence for velocity has been observed for the CVD scheme in physical space. Here, we test this example on the domain shown in Figure 12 using Cartesian perturbed grids honouring the discontinuity shown in Figure 9(c). The numerical pressure field is shown as an isosurface together with pressure contours in Figure 13.

For the cell-wise transform-space control-volume formulation, the numerical pressure convergence is found to be of the order of $h^{0.322}$ for $q=0.1$, $h^{0.848}$ for $q=0.5$ and $h^{0.626}$ for $q=1$, and the numerical velocity convergence was found to be $h^{0.167}$ for $q=0.1$, $h^{0.0873}$ for $q=0.5$ and $h^{0.0943}$

DOI: 10.1002/fld

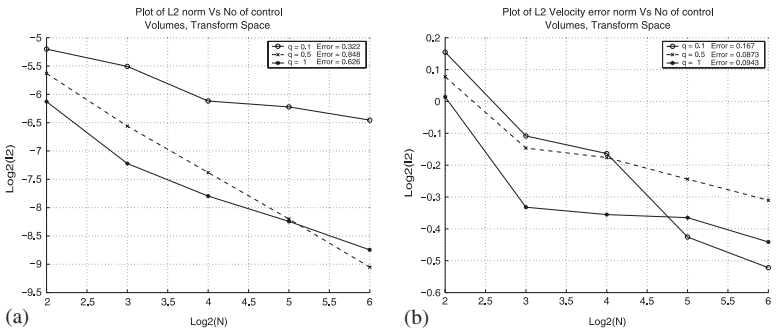

Figure 14. Case 3: (a) pressure convergence for cell-wise transform-space formulation and (b) velocity convergence for cell-wise transform-space formulation.

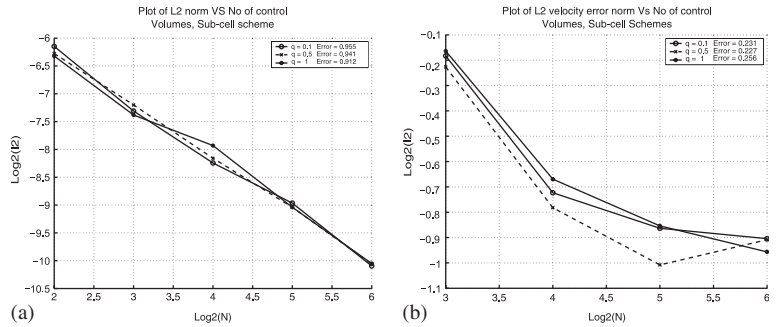

Figure 15. Case 3: (a) pressure convergence for subcell scheme formulation and (b) velocity convergence for subcell scheme formulation.

for $q=1$ as shown in Figure 14. For the subcell transform-space scheme, pressure convergence is found to be of the order of $h^{0.955}$ for $q=0.1$, $h^{0.941}$ for $q=0.5$ and $h^{0.912}$ for $q=1$, and the numerical velocity convergence is found to be $h^{0.231}$ for $q=0.1$, $h^{0.227}$ for $q=0.5$ and $h^{0.256}$ for $q=1$, Figure 15. Pressure and velocity convergences are found to improve when using the subcell space scheme, with convergence in pressure being considerably closer to physical space than the cell-wise scheme. (Physical-space pressure and velocity convergence are shown in Figure 16.) The subcell space results show reduced computational error compared with the cell-wise formulation.

Case 4: A numerical convergence study of the schemes is presented next for a sequence of examples involving a corner-point singularity in the field [26, 34]. The domain is divided into four sub-domains and the permeability tensor is discontinuous across each subdomain boundary as shown in Figure 17(a). The definition of permeability tensor for each subdomain is given in Appendix, for the four cases tested. The numerical solutions are computed on zig-zag grids honouring the discontinuities shown in Figure 9(b). The exact pressure solution is given by

$$\phi(r,\theta)=r^{\alpha}(a_i\sin(\alpha\theta)+b_i\cos(\alpha\theta)) \tag{63}$$

DOI: 10.1002/fld

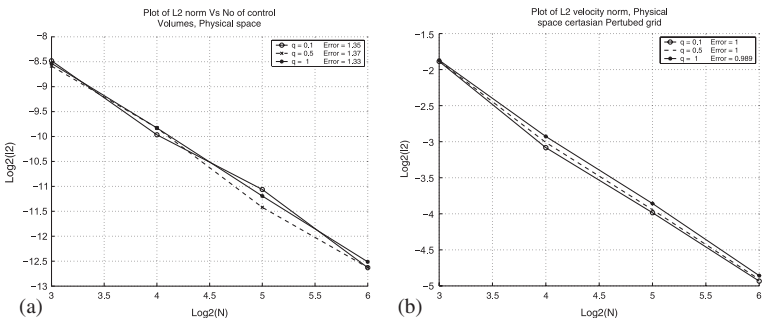

Figure 16. Case 3: (a) pressure convergence for physical-space formulation and (b) velocity convergence for physical-space formulation.

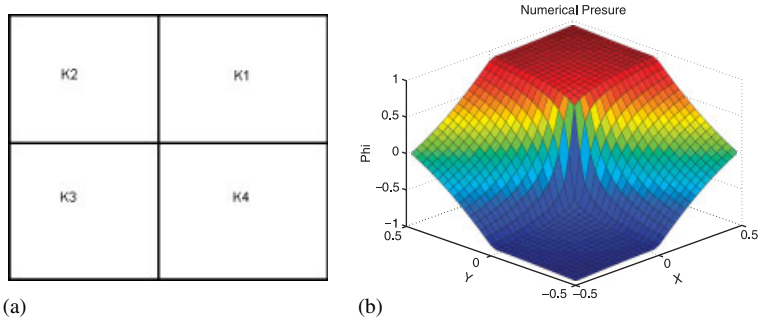

Figure 17. Case 4: (a) subdomain with discontinuity along $\theta=\pi/2$ and (b) subcell pressure solution on the domain.

The difference between problems is in terms of strength of the coefficients and permeability tensor, which also determines the level of difficulty in each case. The higher the value of the parameter α the smoother the test case. More challenging cases arise with decreasing values of α.

9.2. *Case 4.1:* $\alpha=0.53544095$

See Appendix, case 4.1 for the permeability coefficients. The numerical pressure solution using subcell scheme is shown in Figure 17(b). The numerical pressure and velocity convergence for the cell-wise transform-space control-volume formulation are shown in Figure 18.

For the cell-wise transform-space formulation, the pressure convergence is found to be of the order of $h^{0.244}$ for $q=0.1$, $h^{0.228}$ for $q=0.5$ and $h^{0.239}$ for $q=1$. The velocity convergence is found to be of the order of $h^{0.143}$ for $q=0.1$, $h^{0.129}$ for $q=0.5$ and $h^{0.124}$ for $q=1$.

For the subcell scheme the numerical convergence of pressure is found to be of the order of $h^{0.781}$ for $q=0.1$, $h^{0.806}$ for $q=0.5$ and $h^{0.910}$ for $q=1$ and for physical-space formulation, the numerical convergence of pressure is found to be of the order of $h^{1.09}$ for $q=0.1$, $h^{1.1}$ for $q=0.5$ and $h^{1.04}$ for $q=1$, Figure 19. The velocity convergence for the subcell scheme is found to be of the order of $h^{0.205}$ for $q=0.1$, $h^{0.186}$ for $q=0.5$ and $h^{0.175}$ for $q=1$. Again, errors in

DOI: 10.1002/fld

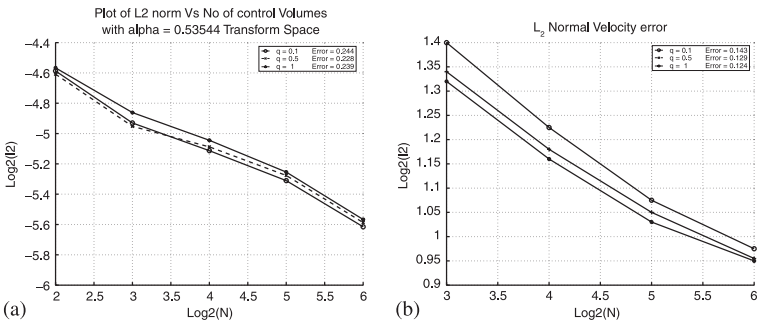

Figure 18. Case 4: (a) pressure convergence for cell-wise transform-space formulation and (b) velocity convergence for cell-wise transform-space formulation.

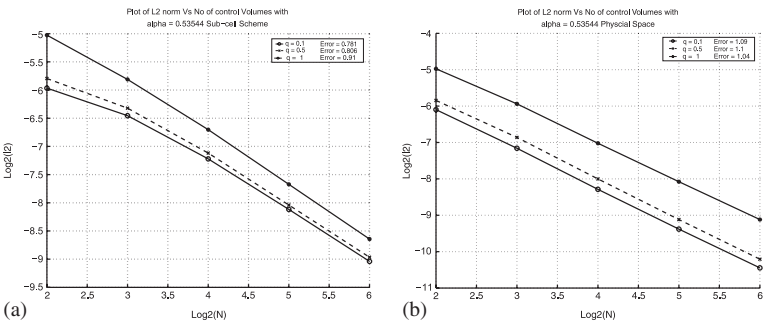

Figure 19. Case 4.1: (a) pressure convergence for subcell scheme formulation and (b) pressure convergence for physical-space formulation.

pressure and velocity are much less in the case of the subcell scheme compared with the cell-wise transform-space formulation.

9.3. Case 4.2: $\alpha = 0.28009739$

In this case (Appendix, case 4.2), the numerical convergence of pressure for the cell-wise transform space formulation is found to be of the order of $h^{0.502}$ for $q = 0.1$ as shown in Figure 20(a) and velocities are found to be diverging. For the subcell scheme the numerical convergence of pressure is found to be of the order of $h^{0.584}$ for $q = 0.1$ (Figure 20(b)) and velocities are diverging. The numerical convergence of pressure for physical-space formulation is shown in Figure 20(c). Again subcell scheme pressure errors are much less than that of the cell-wise scheme and trends in convergence are closer to physical-space pressure results, also $q = 0.1$ yields the best overall performance.

9.4. Case 4.3: $\alpha = 0.1269020697$

This test (Appendix, case 4.3) is of reduced smoothness compared with the previous two test cases because of a smaller value of the parameter α. The numerical convergence of pressure for the

DOI: 10.1002/fld

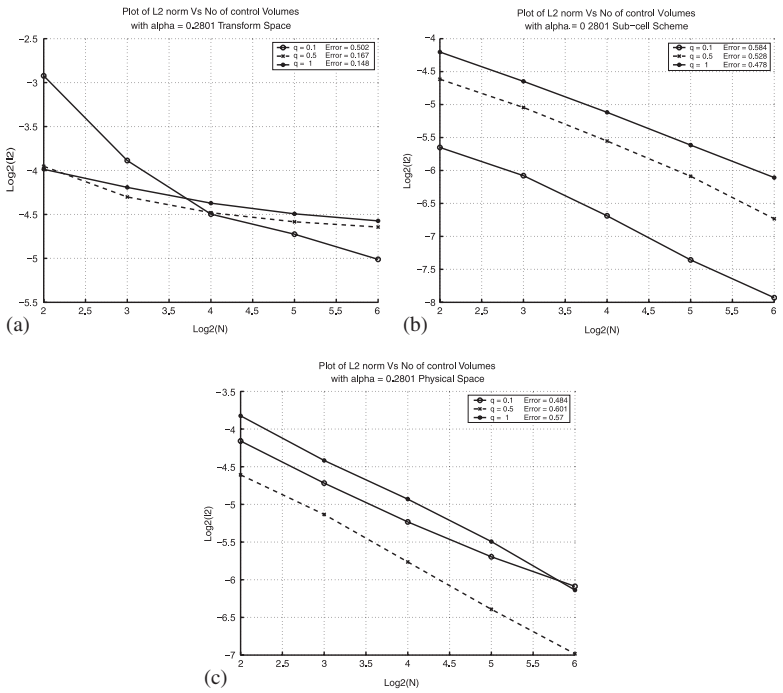

Figure 20. Case 4.2: (a) pressure convergence for transform-space formulation; (b) pressure convergence for subcell scheme formulation; and (c) pressure convergence for physical-space scheme formulation.

cell-wise transform-space formulation is found to be of the order of $h^{0.583}$ for $q=0.1$ as shown in Figure 21(a) and velocities are found to be diverging.

For the subcell scheme, the numerical convergence of pressure is found to be of the order of $h^{0.625}$ for $q=0.1$ (Figure 21(b)), and velocities are found to be diverging. The numerical pressure convergence for physical-space formulation is found to be of the order of $h^{1.04}$ for $q=0.1$; again numerical velocities are found to be diverging [8, 34]. However, as in the previous cases, pressure errors of the subcell schemes are much less than those of the cell-wise schemes and closer in trend to physical-space convergence.

9.5. *Case 4.4:* $\alpha=0.13448835$, $2\pi/3$ *discontinuity*

In the final test case (Appendix, case 4.4 [8]), the domain discontinuity has an orientation at $2\pi/3$ from the horizontal as shown in Figure 22(a). The grid aligned with the interior boundary shown in Figure 9(a) is employed. For this test case, the subcell solution is shown in Figure 22(b). The numerical pressure convergence for the physical-space formulation is shown in Figure 23(a) and pressure convergence for the subcell scheme formulation is shown in Figure 23(b). The numerical velocities are found to be diverging as noted in [8, 34]. Again performance of the cell-wise scheme (not shown) is inferior to the subcell scheme. It can be seen that super-convergence is obtained for $q=0.1$ for both physical and subcell scheme formulations, the scheme is more able to sense

DOI: 10.1002/fld

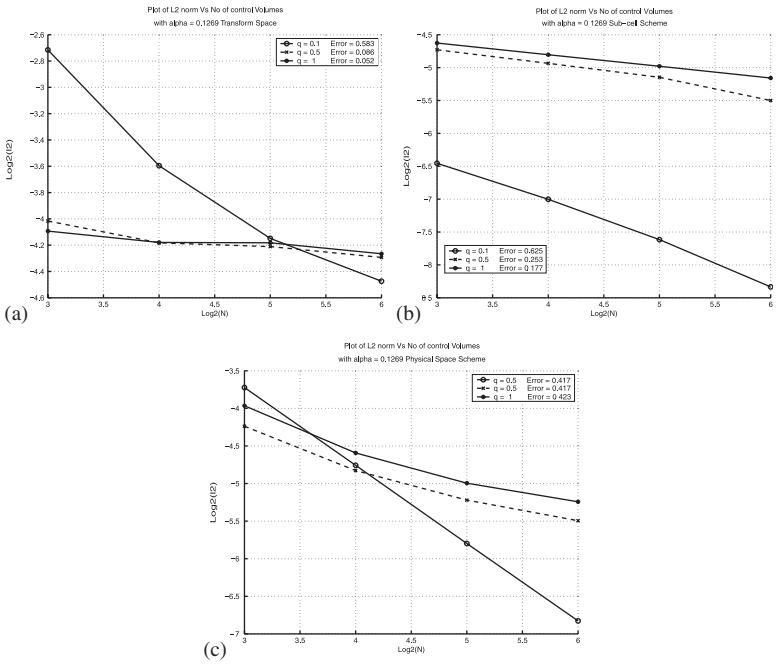

Figure 21. Case 4.3: (a) pressure convergence for transform-space formulation; (b) pressure convergence for subcell scheme formulation; and (c) pressure convergence for physical-space scheme formulation.

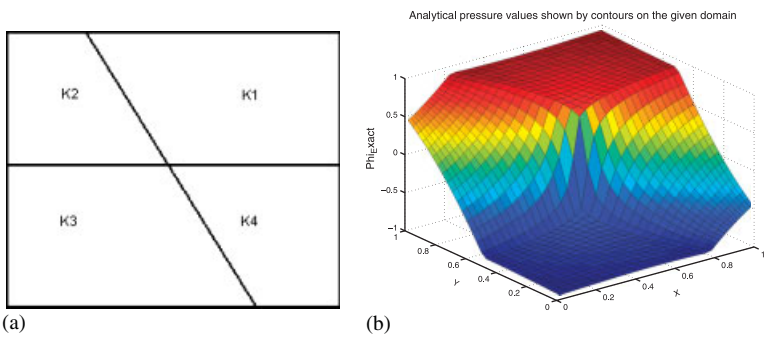

Figure 22. Case 4.4: (a) subdomain with discontinuity along $\theta = 2\pi/3$ and (b) numerical pressure solution.

cross flow as q moves away from the default of unity, consistent with [35]. We also note that physical-space and subcell transform-space convergence rates are quite comparable.

Superior performance of the subcell scheme compared to cell-wise transform space is also obtained for stronger values of α, where subcell errors are found to be significantly smaller. Velocities are found to be diverging in these later cases for physical and transform spaces. We note that the rate of pressure convergence has an exponent less than one in these later cases, since

DOI: 10.1002/fld

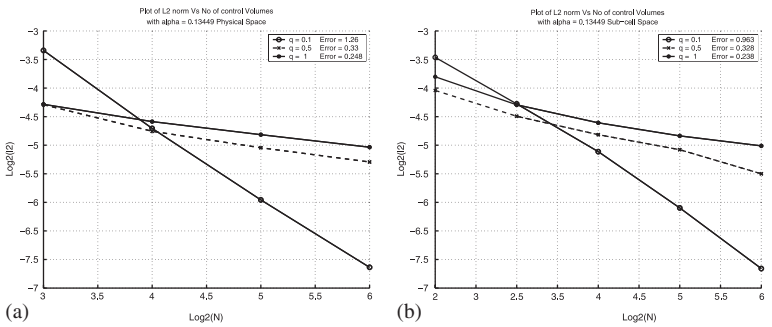

Figure 23. Case 4.4: (a) pressure convergence physical-space scheme and (b) pressure convergence subcell scheme.

velocity is proportional to pressure gradient and can loose an order in convergence, this implies a negative rate as is observed above.

10. CONCLUSIONS

A new family of flux-continuous schemes is defined by the introduction of piecewise constant subcell general-tensor approximations within the formulation. The new formulation is shown to lead to a SPD general-tensor CVD(MPFA) scheme for $q=1$.

While the physical-space schemes maintain exact geometry of the control volumes the physical-space flux matrices are shown to be non-symmetric for general quadrilateral cells and can consequently lead to non-symmetric discretization schemes. The physical-space schemes are also shown to be conditionally positive definite subject to ellipticity of the local symmetric part of the tensor. All test cases presented except $q=0.1$ are found to be positive definite for physical space and transform space.

The relationships between (1) the physical-space q-families, (2) the subcell tensor q-families and (b) the mixed finite element method are given and it is shown that both the CVD(MPFA) schemes (1) and (2) can be recast as mixed methods with special split quadratures.

The effect of subcell tensor approximation and quadrature point on convergence is presented and compared with both the physical-space schemes and the cell-wise transformed control-volume schemes. The subcell schemes use a finer-scale representation of the cell geometry compared with the cell-wise transform scheme and are found to have the better overall convergence performance for the cases tested. In particular, the control-volume face subcell tensor approximation yields the best results of all the SPD schemes. The quadrature point $q=0.1$ is found to be the most beneficial in terms of numerical convergence for the cases tested.

Note that while symmetry is gained for general quadrilateral grids by the subcell schemes together with SPD discretization for $q=1$, the piecewise constant subcell tensor still involves an additional approximation in geometry compared with the physical-space schemes. Consequently, the subcell methods cannot generally retain the accuracy of the physical-space schemes, but consistently improve performance when compared with the earlier cell-wise constant SPD schemes.

DOI: 10.1002/fld

APPENDIX

Case 4.1: $k_1=5, k_3=k_1; k_2=1, k_4=k_1$

$$\begin{aligned}
&\alpha = 0.53544095\\
&a_1 = 0.44721360, \quad b_1 = 2.33333333\\
&a_2 = -0.74535599, \quad b_2 = 1.0\\
&a_3 = -0.94411759, \quad b_3 = 0.5555556\\
&a_4 = -2.40170264, \quad b_4 = -0.481481481
\end{aligned} \tag{A1}$$

Case 4.2: $k_1=k_3=20; k_2=k_4=1$

$$\begin{aligned}
&\alpha = 0.28009739\\
&a_1 = 1.0, \quad b_1 = 0.22360680\\
&a_2 = 2.80952381, \quad b_2 = 2.960396040\\
&a_3 = -0.46485261, \quad b_3 = -0.91318785\\
&a_4 = -4.58039089, \quad b_4 = 0.14148967
\end{aligned} \tag{A2}$$

Case 4.3: $k_1=100, k_3=k_1; k_2=1, k_4=k_1$

$$\begin{aligned}
&\alpha = 0.126902097221\\
&a_1 = 0.1, \quad b_1 = 1.0\\
&a_2 = -9.603960396, \quad b_2 = 2.960396040\\
&a_3 = -0.4803548672, \quad b_3 = -0.8827565925\\
&a_4 = 7.701564882, \quad b_4 = -6.456461752
\end{aligned} \tag{A3}$$

Case 4.4: $k_1=100, k_3=k_1; k_2=1, k_4=k_1$

$$\begin{aligned}
&\alpha = 0.13448835\\
&a_1 = 1.0, \quad b_1 = 0.14177447\\
&a_2 = 4.90138222, \quad b_2 = -13.3407815\\
&a_3 = -0.85392910, \quad b_3 = -0.53935618\\
&a_4 = -9.94074425, \quad b_4 = 10.1578346
\end{aligned} \tag{A4}$$

ACKNOWLEDGEMENTS

The work of the first author was supported by EPSRC grant GR/S70968/01. The second author would like to thank ExxonMobil Upstream Research Company for supporting this project and permission to publish this paper.

DOI: 10.1002/fld

REFERENCES

1. Edwards MG, Rogers CF. Multigrid and renormalization for reservoir simulation. In *Multigrid Methods*, vol. 1, Hemker, Wesseling (eds). Birkhauser: Basel, 1993.
2. Edwards MG, Rogers CF. A flux continuous scheme for the full tensor pressure equation. *Proceedings of the 4th European Conference on the Mathematics of Oil Recovery*, Norway, June 1994.
3. Edwards MG, Rogers CF. Finite volume discretization with imposed flux continuity for the general tensor pressure equation. *Computational Geosciences* 1998; **2**:259–290.
4. Edwards MG. M-matrix flux splitting for general full tensor discretization operators on structured and unstructured grids. *Journal of Computational Physics* 2000; **160**:1–28.
5. Edwards MG. Unstructured, control-volume distributed, full-tensor finite volume schemes with flow-based grids. *Computational Geosciences* 2002; **6**:433–452.
6. Edwards MG. Symmetric positive definite general tensor discretization operators on unstructured and flow based grids. *Eighth European Conference on Mathematics of Oil Recovery*, Freiberg, Germany, 3–6 September 2002.
7. Edwards MG. Control-volume distributed subcell flux schemes for unstructured and flow based grids. *SPE Reservoir Simulation Symposium*, Houston, TX, U.S.A., 3–5 February 2003.
8. Pal M, Edwards MG, Lamb AR. Convergence study of a family of flux continuous, finite volume schemes for the general tensor pressure equation. *International Journal for Numerical Methods in Fluids* 2006; **51**:1177–1203.
9. Lamb AR. Convergence study of a family of nine-point flux continuous, finite volume schemes for the general tensor pressure equation. *M.Sc. Thesis*, University of Wales, Swansea, 2004.
10. Aavatsmark I, Barkve T, Bøe Ø, Mannseth T. Discretization on non-orthogonal, quadrilateral grids for inhomogeneous, anisotropic media. *Journal of Computational Physics* 1996; **127**:2–14.
11. Aavatsmark I, Barkve T, Bøe Ø, Mannseth T. Discretization on unstructured grids for inhomogeneous, anisotropic media. Part I: derivation of the methods. *SIAM Journal on Scientific Computing* 1998; **19**:1700–1716.
12. Aavatsmark I. Introduction to multipoint flux approximation for quadrilateral grids. *Computational Geosciences* 2002; **6**:405–432.
13. Lee SH, Tchelepi H, DeChant LJ. Implementation of a flux continuous finite difference method for stratigraphic hexahedron grids. *Paper SPE 51901. Proceedings of SPE Reservoir Simulation Symposium*, Houston, TX, U.S.A., 14–17 February 1999.
14. Lee SH, Jenny P, Tchelepi HA. A finite-volume method with hexahedral multiblock grids for modeling flow in porous media. *Computational Geosciences* 2002; **6**:353–379.
15. Verma S. Flexible grids for reservoir simulation. *Ph.D. Thesis*, Stanford University, June 1996.
16. Edwards MG. Higher-resolution hyperbolic-coupled-elliptic flux-continuous CVD schemes on structured and unstructured grids in 2-D. *International Journal for Numerical Methods in Fluids* 2006; **51**:1059–1077.
17. Edwards MG. Higher-resolution hyperbolic-coupled-elliptic flux-continuous CVD schemes on structured and unstructured grids in 3-D. *International Journal for Numerical Methods in Fluids* 2006; **51**:1079–1095.
18. Raviart RA, Thomas JM. *A mixed finite element method for second order problems*. Lecture Notes in Mathematics, vol. 606. Springer: New York, 1977; 292–315.
19. Russel TF, Wheeler MF. Finite element and finite difference methods for continuous flows in porous media. In *Mathematics of Reservoir Simulation*, Chapter 2, Ewing RE (ed.). Frontiers in Applied Mathematics. SIAM: Philadelphia, PA, 1983; 35–106.
20. Farmer CL, Heath DE, Moody RO. A global optimization approach to grid generation. *Eleventh SPE Reservoir Simulation Symposium*, Anaheim, CA, U.S.A., 17–20 February 1991; 341–350.
21. Durlofsky LJ. A triangle based mixed finite element finite volume technique for modeling two phase flow through porous media. *Journal of Computational Physics* 1993; 252–266.
22. Arbogast T, Wheeler MF, Yotov I. Mixed finite elements for elliptic problems with tensor coefficients as cell centered finite differences. *SIAM Journal on Numerical Analysis* 1997; **34**(2):828.
23. Russell TF. Relationships among some conservative discretization methods. In *Numerical Treatment of Multiphase Flows in Porous Media*, Chen Z *et al*. (eds). Lecture Notes in Physics, vol. 552. Springer: Heidelberg, 2000; 267–282.
24. Hyman JM, Shashkov M, Steinberg S. The numerical solution of diffusion problems in strongly heterogeneous non-isotropic materials. *Journal of Computational Physics* 1997; **132**:130–148.
25. Riviere B. Discontinuous Galerkin method for solving the miscible displacement problem in porous media. *Ph.D. Thesis*, The University of Texas at Austin, 2000.
26. Riviere B, Wheeler MF, Banas K. Discontinuous Galerkin method applied to a single phase flow in porous media. *Computational Geosciences* 2000; **49**:337–343.

DOI: 10.1002/fld

27. Hughes TJR, Masud A, Wan J. A stabilized mixed discontinuous Galerkin method for Darcy flow. *Computational Methods in Applied Mechanics and Engineering* 2006; **195**:3347–3381.
28. Klausen RA, Winther R. Convergence of multipoint flux approximations on quadrilateral grids. *Numerical Methods for PDE*, submitted.
29. Aavatsmark I, Eigstad GT, Klausen RA, Wheeler MF, Yotov I. Convergence of a symmetric MPFA method on quadrilateral grids. Preprint.
30. Edwards MG, Pal M. Symmetric positive definite subcell CVD schemes on cell-centred quadrilateral grids. *Proceedings of the 10th European Conference on the Mathematics of Oil Recovery*, Amsterdam 4–7 September 2006.
31. Edwards MG, Pal M, Zheng H. Quasi-monotonic variable support $(q1, q2)$ families of continuous Darcy-flux CVD(MPFA) finite volume schemes, submitted.
32. Friis HA, Edwards MG, Mykkeltveit J. Symmetric positive definite flux-continuous full-tensor finite-volume schemes on unstructured cell centered triangular grids. Preprint.
33. Edwards MG, Zheng H. A quasi-monotonic family of continuous Darcy-flux CVD(MPFA) finite volume schemes with full pressure support, submitted.
34. Eigestad GT, Klausen RA. On convergence of multi-point flux approximation o-method; numerical experiment for discontinuous permeability. *Numerical Methods for PDE* 2005; **21**(6):1079–1098.
35. Edwards MG. Superconvergent renormalization and tensor approximation. *Proceedings of the 5th European Conference on the Mathematics of Oil Recovery*, Leoben, Austria, 3–6 September 1996.

DOI: 10.1002/fld